

7-1-2011

MEMS enabled Fabry-Perot cavity for cQED experiments

Francisco Martin Benito

Follow this and additional works at: https://digitalrepository.unm.edu/ece_etds

Recommended Citation

Benito, Francisco Martin. "MEMS enabled Fabry-Perot cavity for cQED experiments." (2011). https://digitalrepository.unm.edu/ece_etds/30

This Thesis is brought to you for free and open access by the Engineering ETDs at UNM Digital Repository. It has been accepted for inclusion in Electrical and Computer Engineering ETDs by an authorized administrator of UNM Digital Repository. For more information, please contact disc@unm.edu.

Francisco M. Benito


Candidate


Electrical and Computer Engineering

Department

This thesis is approved, and it is acceptable in quality and form for publication:

Approved by the Thesis Committee:


_____. Chairperson





**MEMS ENABLED FABRY-PEROT
CAVITY FOR CQED EXPERIMENTS**

by

FRANCISCO MARTIN BENITO

B.S.E.E. UNIVERSIDAD RICARDO PALMA, 1996

THESIS

Submitted in Partial Fulfillment of the
Requirements for the Degree of

**Master of Science
Electrical Engineering**

The University of New Mexico
Albuquerque, New Mexico

May, 2011

©2011, Francisco Martin Benito

Dedication

To Victoria and Verónica, for all their love

To María Andrea and Francisco Lucio, the risk takers

Acknowledgments

First and foremost I offer my sincerest gratitude and appreciation to my advisor, Dr Zayd. C. Leseman, for accepting me to be part of his research group at University of New Mexico. Dr.Leseman has been the pivot and support of my career change. For your patience, encouragement and guide through this thesis and advice to help me to find my ideal job as junior researcher. My deepest gratitude to Dr.Grant Biedermann for the trust offered during this project. My great appreciation for the advice inside and outside the laboratory, his patience to stimulate my intuition in the work done and for the soccer-tennis matches every week. My thanks to Dr. Christos Christodoulou for accepting to be part of my defense committee. Also I would like to express my gratitude to Dr. Kevin Fortier, Dr. Peter Schwindt, Dr. Daniel Stick, Dr. Ihab El-kady and Dr. David Moehring for allow me to work in your group and support me in times of uncertainty in the laboratory. Special thanks also to Dr. Matt Blain for his invaluable help in the design and fabrication of the micro mirrors , to Dr. Yuan-Yu Jau, for sharing his knowledge in electronics, to the members of the laboratory Dr. Cort Johnson, Heather Partner, Rob Cook, George Burns, Thomas Hamilton and former members, Thomas Loyd and Walter Gordy, thanks for your friendship. A very special thanks and recognition to Ian Young for his assistance in the thermal actuator fabrication and former member Dylan Wood , to Drew Goettler for his help in the actuator testing, to Arash Mousavi for his assistance in mirrors cavity and other members of the MTTC lab Khawar Abbas and Maheshwar Kashamolla for the interesting discussions. All this work is dedicated completely to my wife Veronica , who taught me to be a husband, encourage and support me in this drastic turn in my career. To my daughter Victoria, for teaching me to be a father and amaze me everyday with her innocence and savvy. To my parents Maria and Francisco for encouraging me always to do what I love. To my brother, sister and brother-in-law, Daniel, Mirella and Martin for never talking seriously and always laughing at our problems. To all the people who has demonstrated that they are my friends during all the years of my life, Jose Antonio “Ronaldo” Gonzales, Aldo “Chaki” Rios, Ruben “El Huevito” Cedron, Frank Albuquerque, Robert Schardt, Jhonny Martins, Robert DiCrosta, Gabriela Taylor, Daniel Llamocca, Ricardo Otazo, Primitiva Viveros and all the people I met in the bus stop in Lima during my days at school and helped me when I was a kid.

**MEMS ENABLED FABRY-PEROT
CAVITY FOR CQED EXPERIMENT**

by

FRANCISCO MARTIN BENITO

ABSTRACT OF THESIS

Submitted in Partial Fulfillment of the
Requirements for the Degree of

**Master of Science
Electrical Engineering**

The University of New Mexico
Albuquerque, New Mexico

May, 2011

MEMS Enabled Fabry-Perot Cavity for cQED Experiments

by

Francisco Martin Benito

B.S.E.E. Universidad Ricardo Palma ,1996

M.S., Electrical Engineering, University of New Mexico, 2011

Abstract

The development of novel experimental techniques in atomic physics is allowing for the manipulation and control of atoms in structured silicon chips. These new techniques to manipulate atoms in a chip require building micro systems on chip that support actuation, alignment control and tunability for each micro component, which requires a significant integration effort. One example of a new experimental technique in atomic physics is the realization of optical cavities which is a very attractive model for quantum information and communication, because it permits the study of light-matter effects.

The important exigency of an integrated micro cavity consisting of a micro mirror and a fiber optics cable are; alignment between them to form a small cavity volume and actuation to allow for adjustment of the cavity length. In this Master thesis the fabrication of 1-D v-shape or chevron thermal actuator is proposed based on

the following characteristics: the actuator exploits the thermal expansion property of silicon to generate mechanical actuation, offers linear in-plane displacement, large force in small area compared to other actuators schemes and a shuttle that is capable of carrying an optical fiber that creates an optical cavity between it and a micro-mirror. Additionally, fabrication and characterization techniques are also described for the highly reflective (99.9988%) micro-mirrors.

Contents

1	Introduction	1
1.1	Overview	1
1.2	Motivation	2
1.3	Enabling Technology	3
1.4	Objective	4
1.5	Structure of the Thesis	4
2	MEMS Thermal Actuator Theory	5
2.1	MEMS Actuators	5
2.2	Thermal Actuators	6
2.3	Force and Displacement	9
3	Thermal Actuator Fabrication and Characterization	12
3.1	Device Variable Parameters	14
3.2	Device Fabrication Process	15

Contents

3.2.1	Base Material	15
3.2.2	Alignment Forks	16
3.2.3	Device Fabrication	18
3.2.4	Trenches	18
3.2.5	Numerical Analysis	19
4	Cavity Resonators	33
4.1	Cavity Resonators Classical Theory	33
4.1.1	Gaussian Beam	33
4.1.2	Resonator	35
4.1.3	Resonator Types	36
4.1.4	Stability	37
4.1.5	Source of Optical Resonator Loss	39
4.1.6	Resonance Properties of Passive Optical Cavities	40
4.2	Cavity QED System	42
4.2.1	Light and Atom Interaction	42
4.3	Strong Coupling for Open Quantum Systems	44
5	Micro Cavity Characterization	46
5.1	Experimental Setup	46
5.2	Experiment Results	49

Contents

6 Conclusions	57
References	59

Chapter 1

Introduction

1.1 Overview

Advances in Experimental Atomic Physics are allowing the manipulation and control of atoms using microfabrication techniques in silicon. This has opened new challenges in micro fabrication and engineering. During the last two decades physicists have dedicated their efforts to developing techniques and methods to cool and trap atoms. In 1997 Nobel Prize Jury awarded the prize to Steve Chu, Claude Cohen-Tannoudji and William Phillips “for their developments of methods to cool and trap atoms with laser light” [1].

Using laser cooling, trapping techniques and optical cavity technology, it is possible to study the interaction between light and matter through the manipulation of single atoms and single photons. The first experiments of single-atom manipulation were performed in ion traps. Ion traps are systems which are comprised of a static and oscillating electric field as suggested by Wolfgang Paul who won the Nobel Prize in Physics in 1989 for this work. Ion traps keep an ion confined to a region of space.

Using photons, ions can be cooled in the trap and detected.([2],[10])

Another crucial experiment is that emerged in the 1970's, confined photons in a cavity with high reflectivity mirrors and atoms. Then the atoms can be sent into the cavity to interact with the light. This experiment belongs to the category of Cavity Quantum Electrodynamics (cQED).

Of particular importance in this type of experiment is the ability of the photons to imprint information about the field state of the atom during these interactions with each other without destroying the photon. Because of this capability, the study of cQED experiments has profound interest in the area of quantum information. This is the main motivation for this work.

1.2 Motivation

Most cQED experiments performed during 1980's and 1990's were are the macroscopic scale. In recent years advances in miniaturization have gained popularity and attempts to integrate open micro cavities in a chip have been demonstrated using different techniques. One of these basic techniques developed by Hinds[12]demonstrated the optical detection of single atoms using two optical fibers to form a micro cavity. The Reichel[26] Group in France embedded this design attaching a concave dielectric mirror to the optical fiber to form a Fabry Perot cavity mounted on a chip. Purdy and Stamper-Kurn[22] mounted a small planar mirror micro fabricated on a sapphire substrate and a curved mirror suspended above the chip to shape a vertically oriented Fabry-Perot resonator.

Trupke [27] proposed an open cavity which consisted of a concave micro-mirror and the plane tip of an optical fiber, both coated for high reflectivity. Concave micro-

mirrors were fabricated on a silicon substrate using a standard wet-etching isotropic process to control the radius of curvature of each micro-mirror. Gold was sputtered onto the micro-mirrors to increase their reflectivity. A plane dielectric multilayer mirror was fabricated and transferred to the optical fiber tip.

A method similar to Trupke's approach is followed in this work. In particular, this approach complies with the Cavity QED requirements of a strong coupling regime and forms a very small volume cavity with high finesse. Moreover, it involves standard optical coating techniques and standard silicon etching which is highly repeatable. Additionally, this approach includes integrated actuators for tuning and mode selection in order to avoid external tuning by piezoelectric devices.

1.3 Enabling Technology

Micro Electro-Mechanical Systems (MEMS) are bringing the opportunity to fabricate miniaturized devices on a silicon substrate using standard semiconductor fabrication techniques. As previously describe in Section 1.1 physicists have achieved a strong knowledge of how to interact atoms with photons. The confluence of these two areas create the opportunity to begin performing quantum experiments at the micro scale.

Improvements in alignment between a micro mirror slab and an optical fiber are necessary. A MEMS actuator fabricated to pull an optical fiber cable which varies the distance between this cable and the high reflectivity mirror allows for the creation of an adjustable Fabry-Perot cavity. The mirror needs to have micro scale dimensions globally and a surface roughness on the order of Angstroms in order to create a high finesse Fabry Perot cavity. A key issue to overcome in this work is that of alignment between the fiber and mirror.

1.4 Objective

This thesis will propose a technique to solve the issues stated previously. Ultra smooth micro-mirrors with high reflectivity coating will be fabricated using a combination of isotropic dry etches followed by optical coatings. These micro-mirrors will be characterized as part of a Fabry-Perot cavity. A MEMS thermal actuator is proposed to solve the issue of alignment and tuning of the cavity length. The proposed thermal actuator consists of chevron shape arms carrying a shuttle on the center of the device where the optical fiber will rest. The MEMS actuator will be constrained to 1-D motion in order to tune the cavity length and mode.

1.5 Structure of the Thesis

The outline of each chapter is the following: Chapter 2 presents the MEMS thermal actuator theory with emphasis to the force and displacement calculation needed to device design. Chapter 3 gives a detailed MEMS thermal actuator fabrication procedure and characterization. Chapter 4 introduces the classical theory of cavity resonators and the strong coupling concept required to understand the cavity design and results. Chapter 5 explains the method and results for the cavity mirrors' characterization. Chapter 6 presents conclusions and future experiments for this work.

Chapter 2

MEMS Thermal Actuator Theory

This chapter illustrates the different classes of MEMS actuators, its advantages over force and displacement characteristics. Also, it explains why the thermal actuator was chosen as the best alternative for the optical fiber actuation. Finally, equations for the force and displacement of the thermal actuator are derived and analyzed.

2.1 MEMS Actuators

Micro Electro-Mechanical Systems (MEMS) Technology, is the integration of mechanical elements, sensors and actuators, and electrical signals on a common silicon substrate, using micro fabrication techniques similar to the ones used in semiconductor electronics fabrication. Within this broad spectrum of electro mechanical elements; actuation occupies a special place in research and development of integrated systems [3].

MEMS actuators consist of five types of families: electrostatic, piezoelectric, thermal, magnetic and optical. Each of them is subdivide into classes. All these families

have different characteristics and advantages depending on engineering application. Electrostatic actuators have a force output lying mid-range at 10^{-6} N to 10^{-3} N, but offer large displacements of up to $200 \mu\text{m}$ [6]. To reach this range of force, the electrostatic actuators require high operating voltages on the order of 100 volts [20]. Additionally, they occupy relatively large area in the chip [24]. In the case of electromagnetic and magnetic actuators, the displacement and force generated are relatively small. These forces are in the range of 10^{-7} N to 10^{-6} N and the small displacements in the range of 10^{-5} m to 10^{-3} m have been achieved [17]. For piezoelectric actuators the maximum force generated, is typically between 10^{-5} N and 10^{-3} N and the maximum displacement between 10^{-7} m and 10^{-3} m.

Thermal actuators are capable of producing relatively large forces in comparison to other types of actuators. They are based on generation of temperature differentials and thermal expansion.

The system proposed in this thesis requires high force and small displacement that can be controlled with low drive voltage. Thermal actuators comply with these constraints and are the best suited for this application.

2.2 Thermal Actuators

Thermal actuators take advantage of the basic effect of thermal expansion, which is, the tendency of a material to increase its volume in response to an increase in temperature change ΔT . Mathematically for a linear model, its change in length ΔL can be predicted by [13]:

$$\Delta L = L\alpha\Delta T \tag{2.1}$$

where α is the coefficient of thermal expansion of the material, in this case silicon. The coefficient of thermal expansion itself is a function of temperature. It is not

Chapter 2. MEMS Thermal Actuator Theory

constant over all temperature ranges. A precise determination of thermal expansion coefficient of silicon between 300 K and 1500 K was given by Okada and Tokumaru [21]

$$\alpha_I = [3.725 \times (1 - e^{-5.88 \times 10^{-3}(T-125)} + (5.548 \times 10^{-4})T)] \times 10^{-6} \quad (2.2)$$

In order to cause thermal expansion in a silicon beam, an electric current will be applied between the ends of the silicon beam. The current flowing through it, will cause it to heat via Joule Heating, thus causing it to expand. The amount of heat generated is proportional to the product of square of the electric current and the electrical resistance.

$$Q \propto I^2 \cdot R \quad (2.3)$$

Moreover, the electrical resistance is proportional to the length of the conductor multiplied by electrical resistivity and inversely proportional to the cross sectional area of the beam.

$$R = \rho \frac{\ell}{A} \quad (2.4)$$

Clearly geometry plays an important role in the generation of force. However, displacement is insensitive to the cross sectional area of beam and to the number of parallel silicon beam [5]. The two ends of the beam are typically constrained in a manner that causes the beams to displace or deflect in a controlled manner, typically 1-D motion. The outcome creates mechanical actuation which can be amplified through different geometric configurations.

Thermal conductivity, is a property of materials that indicate its ability to transfer heat. In order to accurately model the deflection of the beam the thermal conductivity as a $\kappa(T)$ must be know. The thermal conductivity of polysilicon is [18]

[5]:

$$\kappa_p = \frac{1}{-2.2 \times 10^{-11}T^3 - 9 \times 10^{-8}T^2 - 1 \times 10^{-5}T + 0.014} \quad (2.5)$$

And for air [11]

$$\kappa_a = 3.4288 \times 10^{-11}T^3 - 9.1803 \times 10^{-8}T^2 + 1.2940 \times 10^{-4}T - 5.2076 \times 10^{-3} \quad (2.6)$$

As this equation indicates, the thermal conductivity is in function of temperature. Hence, if the temperature increases, the thermal conductivity will increase as well. To calculate the amount of Joule heating, one needs to know the material resistivity, which depends of the concentration of the dopants. The resistivity value for polysilicon at room temperature is a readily available value, because its long time prominence in the semiconductor industry. However, the resistivity value is variable with respect to the temperature. Baker et al. measured the resistivity in a range of temperature and determined the following relations between temperature variation and resistivity of the polysilicon[5]:

if $T < 300$

$$\rho = 2.9713 \times 10^{-2}T + 20.858 \quad (2.7)$$

if $T > 300$ and $T < 700$

$$\rho = 6.16 \times 10^{-5}T^2 - 7.2473 \times 10^{-3}T + 26.402 \quad (2.8)$$

if $T > 700$

$$\rho = 8.624 \times 10^{-2}T - 8.8551 \quad (2.9)$$

where the temperature is in degrees Celsius.

Another important property of the material is the modulus of elasticity(Young's Modulus), which is used to calculate the amount a beam will extend under tension or the load at which the beam will buckle under compression. For polysilicon it has been measured to be 164.3 ± 3.2 GPa [16]and for single crystal silicon in [110] 168 GPa[4].

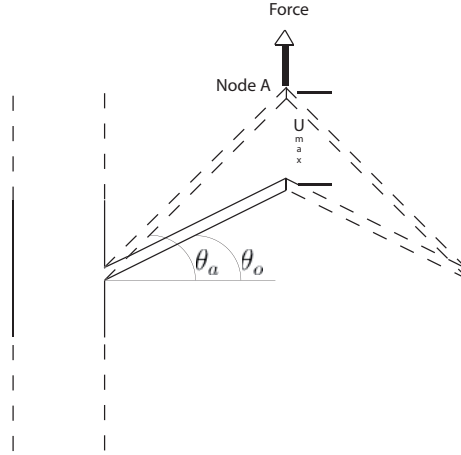


Figure 2.1: Arm Enlogation Analysis

2.3 Force and Displacement

In order to measure the displacement of node A in Figure 2.1, the elastic stiffness matrix method was followed [28]. By symmetry, an arm of the V shaped, or chevron, actuator is used as reference for analysis. Bending and tension are calculated and introduced in the stiffness matrix.

The beam acts as the reference axis with an inclination angle θ . As is shown in Figure 2.1, the beam is going to be displaced along these axes.

The elongation of the beam is generated by the thermal stress on the beam, which can be considered to be due to the average temperature increase along the length of the beam. The thermal stress can be calculated using the coefficient of thermal expansion of the material α , Young's Modulus of the material E , and the average increase of temperature, ΔT .

$$\sigma = \alpha \Delta T E \quad (2.10)$$

The stress is equal to the average force exerted over unit area. Hence, the average force exerted by the arm in V-shape case is equal to the thermal stress times area of

the beam cross section.

$$F = \alpha\Delta TEA \quad (2.11)$$

The total force on the beam is equal to the stiffness multiplied by the displacement or deflection produced by the thermal force and reaction at the node. Therefore, the elastic stiffness matrix can be represented by:

$$\begin{bmatrix} \frac{EA}{l} & 0 \\ 0 & \frac{12EI}{l^3} \end{bmatrix} \begin{bmatrix} U_{x'}^A \\ U_{y'}^A \end{bmatrix} = \begin{bmatrix} \alpha\Delta TEA \\ 0 \end{bmatrix} + \begin{bmatrix} R_{x'}^A \\ R_{y'}^A \end{bmatrix} \quad (2.12)$$

where I is the moment of inertia, l is the beam length, $R_{x'}^A$ and $R_{y'}^A$, are the reaction forces in both directions and $U_{x'}^A$ and $U_{y'}^A$ is the displacement in both directions.

As is stated above for convenience, the beam's axis is the axis of reference. All matrices need to be rotated to the X-Y plane to apply the boundary conditions. The clockwise rotation matrix is represented by:

$$\begin{bmatrix} \cos \theta & \sin \theta \\ -\sin \theta & \cos \theta \end{bmatrix} \quad (2.13)$$

Applying rotation to the stiffness matrix¹:

$$\begin{bmatrix} c^2 \frac{EA}{l} + s^2 \frac{12EI}{l^3} & cs \left(\frac{EA}{l} - \frac{12EI}{l^3} \right) \\ cs \left(\frac{EA}{l} - \frac{12EI}{l^3} \right) & s^2 \frac{EA}{l} + c^2 \frac{12EI}{l^3} \end{bmatrix} \begin{bmatrix} U_x^A \\ U_y^A \end{bmatrix} = \begin{bmatrix} \alpha\Delta TEAc \\ \alpha\Delta TEAs \end{bmatrix} + \begin{bmatrix} R_x^A \\ R_y^A \end{bmatrix} \quad (2.14)$$

Analyzing the beam at node A, there is no displacement along the x axis, but there is along the y axis; conversely there is a reaction on the x axis, but not the y axis. Applying these boundary conditions to the rotated stiffness matrix in $x - y$ plane, and solving for displacement in y direction caused by a temperature increment.

$$U_y^A = \alpha\Delta Tl \frac{\sin \theta}{\sin^2 \theta + \frac{12I \cos^2 \theta}{Al^2}} \quad (2.15)$$

¹ $\cos \theta$ and $\sin \theta$ will be represented by c and s respectively in the resulting matrix

Chapter 2. MEMS Thermal Actuator Theory

If the total force generated by the temperature variation and reaction is replaced by an external force at node A, acting only y direction, the displacement can be calculated substituting the total force by $\frac{F}{2}$:

$$U_y^A = F \frac{1}{2 \left(\frac{EA \sin^2 \theta}{l} + \frac{12EI \cos^2 \theta}{l^3} \right)} \quad (2.16)$$

from this equation the stiffness of the V-shape beam is equal to:

$$K = \frac{F}{U_y^A} = 2 \left(\frac{EA \sin^2 \theta}{l} + \frac{12EI \cos^2 \theta}{l^3} \right) \quad (2.17)$$

After a current is applied on its ends, the apex on the V shape is going to move outward in plane a known distance if the temperature is known. The blocking force needed to move the apex back to its rest position is equal to [23]:

$$F_{max} = \int_{\theta_a}^{\theta_o} K dY \quad (2.18)$$

The displacement is a function of the bending angle θ is equal to:

$$Y = l \sin \theta \quad (2.19)$$

The stiffness found above varies in function of the bending angle θ

$$F_{max} = 2EA \left[\frac{\sin \theta_a - \sin \theta_o}{\psi} - \frac{(1 - \psi)(\sin^3 \theta_a - \sin^3 \theta_o)}{3\psi} \right] \quad (2.20)$$

where θ_o is the bending angle when the actuator is at rest and θ_a is the angle when the actuator goes to a maximum displacement at a known temperature and $\psi = \frac{Al^2}{12I}$. θ_a is related to θ_o and U_y^A by

$$\theta_a = \sin^{-1} \left(\sin \theta_o - \frac{U_y^A}{l} \right) \quad (2.21)$$

Note that θ_a is a function of the displacement generated by the average increase in temperature.

Chapter 3

Thermal Actuator Fabrication and Characterization

In chapter 2 the theory for modeling of chevron type thermal actuator was outlined. This type of thermal actuator allows linear motion of the device, control of the arms displacement and creates larger mechanical force compared to the micro electro static actuators. The thermal actuator has several additional features consisting of:

- Shuttle, this is a free hanging structure that carries the fiber optic cable and is held by the expansion arms.
- Backbone, is a fix piece located behind the shuttle, used to align the fiber optic in the trench that runs through both the shuttle and this structure.
- Trench, is located in the top of the shuttle and backbone, which allows for mounting and alignment of the fiber optic cables.
- Arms, are the components that connect the anchor pads to the shuttle. The arms expand when heated causing the shuttle to move in one direction.

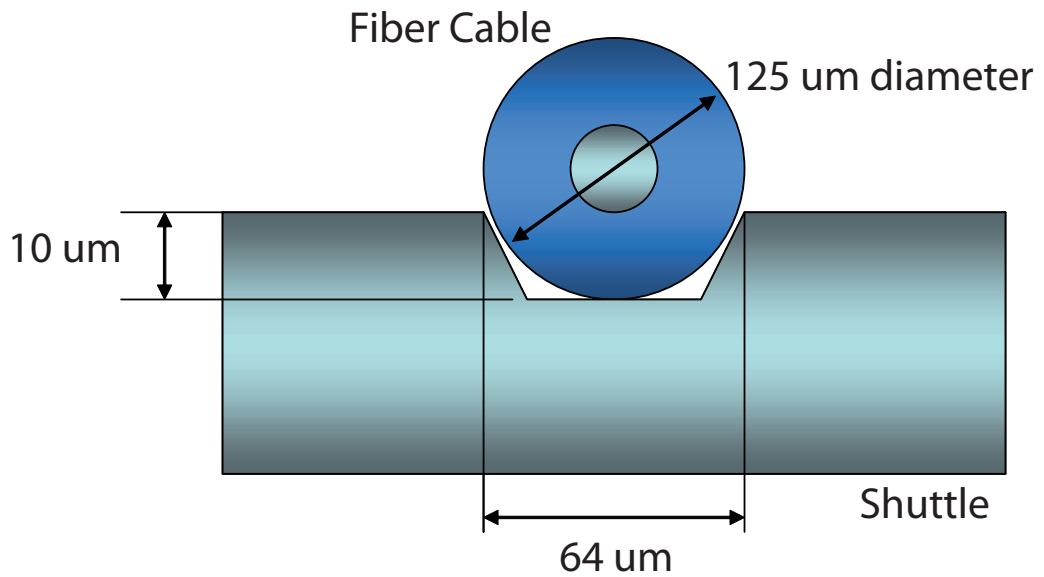


Figure 3.1: Shuttle with Fiber Optics Cable

- Anchor Pad, is where the voltage drop is applied to pass current to the actuator arms and serves as support for one end of the actuator arms.

In Figure 3.1, the shuttle trench width was determined having consideration that the optical fiber is going to have contact only on the trench walls. To accomplish this, a gap (h) of $1.0 \mu\text{m}$ was employed. Setting the trench depth, $d + h$ equal to $10 \mu\text{m}$, or half of the shuttle thickness, and the fiber optics cable of a diameter of $125 \mu\text{m}$ gives a minimum trench width of $64 \mu\text{m}$. A tangent between the circle and shuttle makes an angle of 32.5° with the horizontal. This is much smaller than the anisotropic etch angle of 54.7° for the silicon crystal. Therefore, the optical fiber will make contact with the upper corner of the trench as shown in the Figure 3.1, not with any point on the trench. The shuttle must extend $1000 \mu\text{m}$ beyond all other features making the shuttle length equal to $2900 \mu\text{m}$ with a width of $130 \mu\text{m}$. Release holes of $10 \times 10 \mu\text{m}$ and spaced $10 \mu\text{m}$ apart are added in the shuttle. Anchors are $1520 \mu\text{m}$ by $1520 \mu\text{m}$.

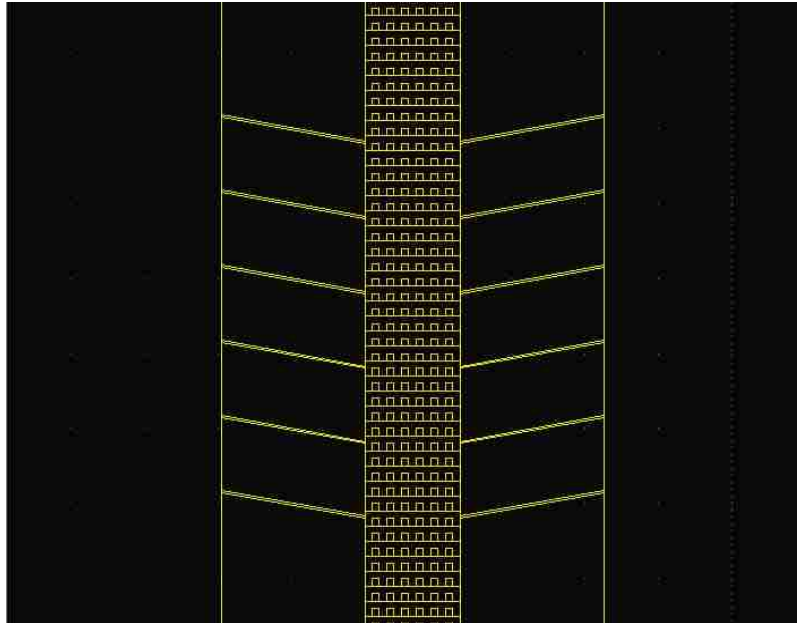


Figure 3.2: Computer Aided Design of Device

3.1 Device Variable Parameters

Three different types of thermal actuators consisting of 2, 4, and 6 pairs of arm with varying angles and different arm widths showed in Fig 3.3 were built. A number of 72 different actuators were patterned on a 6 inch wafer. The main requirement is a device that can output enough force to move the fiber optics cable in a linear fashion.

- The arm angle sets maximum range of distance the actuator can move at the expense of the resolution the actuator is able to achieve. The steeper the angle, the farther the actuator is able to move per increase in current applied.
- The number of set of arms on the devices affect the amount of output force of the actuator. The higher the number of arms the larger force the actuator is able to create.

- The arm width increasing also increase the output force of the actuator. Moreover the arm width affects the resistivity of the arms and hence limiting the amount of current that can be passed through arms before they fail.

Referring to Table 3.1, the top row are arm angles, the left most column has the number of pairs of arms, and the middle are values of arm widths. For instance, the first device in the top left most space has two pairs of arms, angled 5° from the horizontal and the arms are $5 \mu\text{m}$ wide.

3.2 Device Fabrication Process

The device fabrication can be split in three processes, based on the number of features that have to be patterned in the silicon wafer. Two masks are needed to fabricate the device in silicon. First mask consists of the alignment cross hairs features for alignment to the crystallographic planes of the wafer and had trenches of dimensions equal to $64 \mu\text{m}$ by $2560 \mu\text{m}$. The second mask consists of 72 devices with varying arm width, length and gap as were described in the previous section. First, building the alignment forks, second building the trenches and finally building the main pattern in the device.

3.2.1 Base Material

6 inch Silicon On Insulator (SOI) wafers are used to the device fabrication. SOI wafers consist of a $600 \mu\text{m}$ thick on the top, a $3 \mu\text{m}$ thick SiO_2 layer that is used as sacrificial layer, and a $20 \mu\text{m}$ thick silicon device layer. An additional masking layer of SiO_2 is added to the wafer using a tube furnace, a quartz tube with tube hook ups at the end for gas flow, and a flow regulator. Wafers are placed within the tube.

Argon gas is flowed over the wafers as the furnace heats them to 1100°C . Once the furnace has reached its set temperature, the argon flow is shut off and oxygen is flowed through forming a solid film. $1\ \mu\text{m}$ of silicon dioxide is grown on the wafer using this technique. The added layer of SiO_2 is used as a mask for the two KOH etch steps that used to pattern the alignment forks and the trenches. It is because, photoresist has an etch rate lower than the KOH etch rate. KOH etches around $1100\ \frac{\text{nm}}{\text{min}}$ of silicon versus around $17900\ \frac{\text{nm}}{\text{min}}$ for S1822 positive photoresist. This shows clearly that the mask would be gone long before the KOH etched the patterned feature. On the other hand, the etch rate of SiO_2 is only $7\ \frac{\text{nm}}{\text{min}}$.

3.2.2 Alignment Forks

The alignment forks are the first feature imprinted on the top of the wafer. It will be used as reference pattern for the other features that are going to be added to create the thermal actuator device. The wafer preparation starts with de-scumming process to promote adhesion performed in tool March RIE etcher for 60 seconds. It is moved to a dehydration bake hot plate to 112°C for 5 min. At this point wafer is ready to begin with alignment marks fabrication process. The wafer is placed on CEE Coater tool to be spin to 4000 rpm for 10 sec. with HMDS (hexamethyldisilazane). HMDS is an adhesion promoter used to enhance the bonding of photo resist to a silicon dioxide surface. Keeping the wafer on the CEE tool AZ 1518 photoresist is poured and wafer spin to 4000 rpm for 20 sec. The silicon wafer is soft baked on hot plate at 110°C for 90 sec to remove some of the solvent in the resist and make the resist more viscous. The wafer is moved to the Karl Suss tool to continue with the exposure process. Since this is the first step on fabrication process, alignment is not necessary and mask image is projected on resist using ultraviolet light for 5 sec to cause selective chemical property change.

A preparation of H_2O and AZ400K developer (4:1) is poured in a vessel in the caustic bench to obtain high resolution from the concentrate. The wafer is immersed into the developer bath for 5 min. Immediately after a dump rinse is done and spin rinse dry performed in the Verateq tool. Descumming is performed again to remove thin layer of resist scum that may obstruct open regions on pattern. The pattern is transferred to the SiO_2 using deep reactive ion etching which is a highly anisotropic etch used to create deep, steep side trenches. The wafer is transported to de scumming tool to expedite sulfuric dissolving photo resist for 60 sec. Piranha acid is used to remove all photo resist in order for KOH to uniformly etch SiO_2 at $100^\circ C$ for 20 min. The wafer is now placed in a vessel with Potassium Hydroxide (KOH) at $80^\circ C$ for 15 min. Dump rinse with water and Spin-Rinse Dry in the Verateq tool is completed. The result is shown in the Figure 3.6 below the alignment fork is etched symmetrically. It will be used as alignment patterns during the fabrication of the trenches and arms. The alignment forks are used to align the wafer and the mask to the $[1\ 1\ 0]$ direction in order to pattern the trenches by observing the symmetry of the forks. If the wafer and the mask were not aligned to the $[1\ 1\ 0]$ direction, the trench shape would have a shape different to the trapezoidal trench desired. It was also found that the lateral etch rate of the $\langle 1\ 1\ 1 \rangle$ planes are very sensitive to the angular misalignments. The etch rates increase by a factor of approximately 2 for a misalignment of 1° .

3.2.3 Device Fabrication

3.2.4 Trenches

A very similar process is followed to fabricate the trenches. The trenches are first patterned in photoresist. Once again, the wafer is laid in a hot plate at $110^\circ C$ for 5 min for dehydration bake to aid resist adhesion and descumming for preparation

Chapter 3. Thermal Actuator Fabrication and Characterization

before the HMDS and AZ 1518 PR coating. This time the photoresist is spun at 4000 rpm for 20 sec with the HMDS and PR coating, followed by soft bake in hot plate at 110°C for 90 sec. In the Karl Suss tool the wafer and mask are aligned to the [1 1 0] direction in the mask aligner tool with the aid of the alignment forks. The most symmetric fork on either side of the wafer is found by using the two microscopes on the mask aligner tool. Ultra violet light exposed on the photo resist for 5 sec. In order to remove the photoresist that was not exposed , the wafer is immersed in the H_2O :AZ400K developer solution for 4 min. Wafer is a new dump rinse and spin rinse dry for 5 min. The pattern is transferred through the SiO_2 mask down to the device layer using Adixen DRIE tool and a 4.5 min SiO_2 etch. After transferring the pattern down to the device layer, the photoresist mask is removed in preparation for etching the trenches in KOH.

The trenches are etched down 10 μm into the device layer. The bath was heated to 80 °C and the concentration of KOH used was 45 wt% KOH. The etch rate is highly dependent on the temperature of the bath. The higher the temperature of the bath, the higher the etch rate of the bath. The reason the bath temperature is set to 80°C is that the etch produces a uniform and bright surface at this temperature. Non-uniformity of the etch rate becomes considerably worse above 80 °C. It was found that it took longer to etch down to 10 μm because, despite covering the bath with a watch glass, a significant amount of evaporation occurred during the etch causing the etch rate to slow. It took around 14 min to etch the trenches down to 10 μm .

Since the angle between the $\langle 100 \rangle$ plane and the $\langle 111 \rangle$ plane is 54.74° we can find the depth of the trench-using trigonometry. A cleaved picture of a trench is shown below in Figure 3.11. This wafer was not an SOI, but a bulk Si test wafer. After etching the trenches and removing the SiO_2 mask the devices are patterned

over the trenches as shown in the Figure 3.12. In order to avoid a non uniform PR layer, a thicker viscosity resist (AZ 9260) was used. The PR was deposited on the wafer to a speed of 50 rpm. After patterning the devices in PR, the pattern is transferred through the device later on the sacrificial SiO_2 layer using a 15 minute DRIE Si etch and remove the photoresist using a piranha bath. Once the devices are patterned in silicon, the last step of the fabrication process is to etch away all the SiO_2 underneath the shuttle and the arms to release the movable structure. This sequence of steps is shown in Figures 3.9-3.13. Fig 3.14 is that of a completed device.

3.2.5 Numerical Analysis

The numerical model is depicted in Fig. 3.14. It is comprised of two pads, six legs and a shuttle as is shown in Fig.3.15. The simulation is performed in ANSYS [14]. In the current Finite Element Analysis, the element solid98 is used with 10 nodes. Each node has five degrees of freedom, including three deflections, temperature and voltage. The FEA simulates the thermal actuator in a field coupling electric, thermal and elastic analysis. A small area at the center of each pad is subjected to a constant voltage consistent with the applied voltage in the actual wire bonds. Moreover, the temperature on the surfaces underneath the pad is kept at ambient temperature to model the heat sink behavior of the substrate. Since the thermal actuator is anchored to the substrate, the nodes on the corresponding areas are mechanically fixed. As show in Fig. 3.15, the simulation returns the distribution of the temperature.

In a thermo-elastic analysis, this distribution of temperature is used as body forces to calculate the displacement of the shuttle as is shown in Fig. 3.16. Since the thermal expansion ratio and thermal conductivity if silicon depend on temperature this analysis is not linear. However, the effects of large displacements, radiation

Chapter 3. Thermal Actuator Fabrication and Characterization

and convection are ignored. The Young's modulus of silicon is assumed 160 GPa which do not vary with the temperature significantly. The analysis shows that the temperature doesn't exceed 1000 K within the applied range of the voltages.

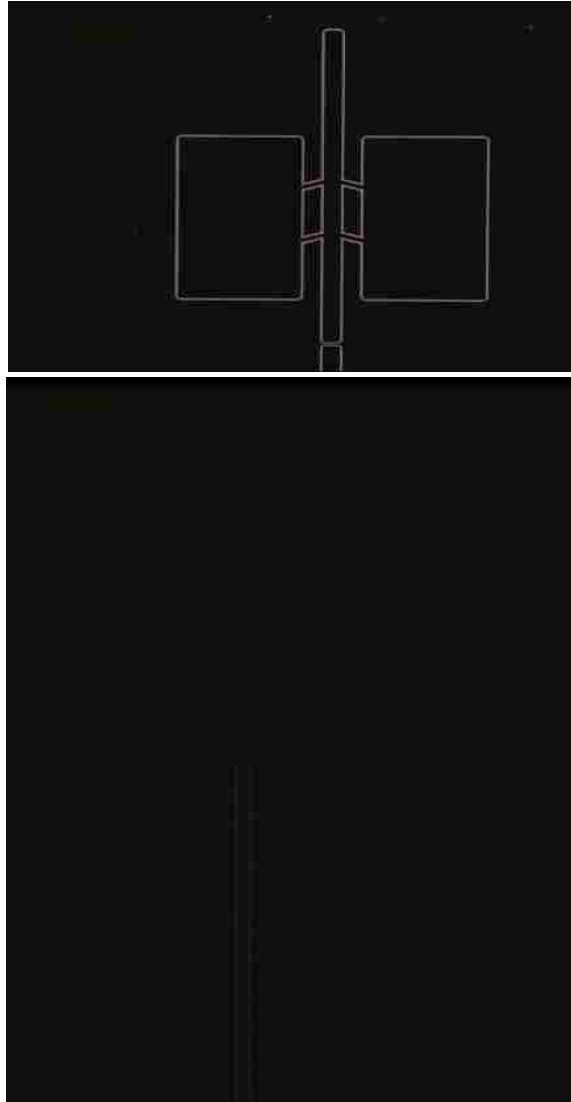


Figure 3.3: Thermal actuators as fabricated

Chapter 3. Thermal Actuator Fabrication and Characterization

Arm angle	5°	10°	15°	20°	25°	30°	5°	10°	15°	20°	25°	30°
Number of pairs of arms	Arm widths in microns											
2 arms	5μm	5μm	5μm	5μm	5μm	5μm	10μm	10μm	10μm	10μm	10μm	10μm
4 arms	5μm	5μm	5μm	5μm	5μm	5μm	10μm	10μm	10μm	10μm	10μm	10μm
6 arms	5μm	5μm	5μm	5μm	5μm	5μm	10μm	10μm	10μm	10μm	10μm	10μm
2 arms	3μm	3μm	3μm	3μm	3μm	3μm	20μm	20μm	20μm	20μm	20μm	20μm
4 arms	3μm	3μm	3μm	3μm	3μm	3μm	20μm	20μm	20μm	20μm	20μm	20μm
6 arms	3μm	3μm	3μm	3μm	3μm	3μm	20μm	20μm	20μm	20μm	20μm	20μm

Figure 3.4: Table describing the different arm widths and the number of arms in the device



Figure 3.5: Wafer with device pattern in photoresist

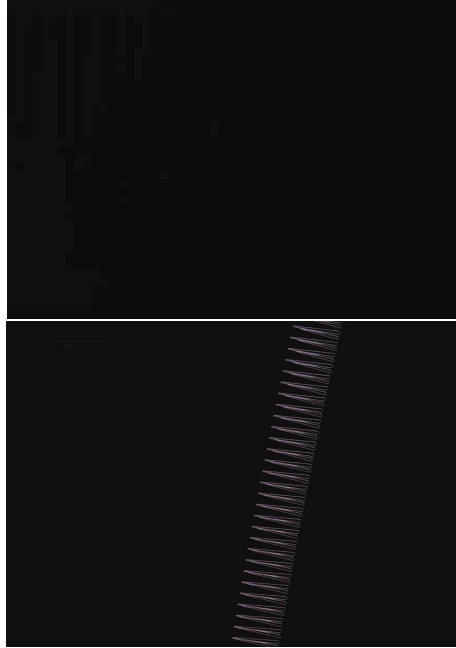


Figure 3.6: Align Forks on the Si wafer

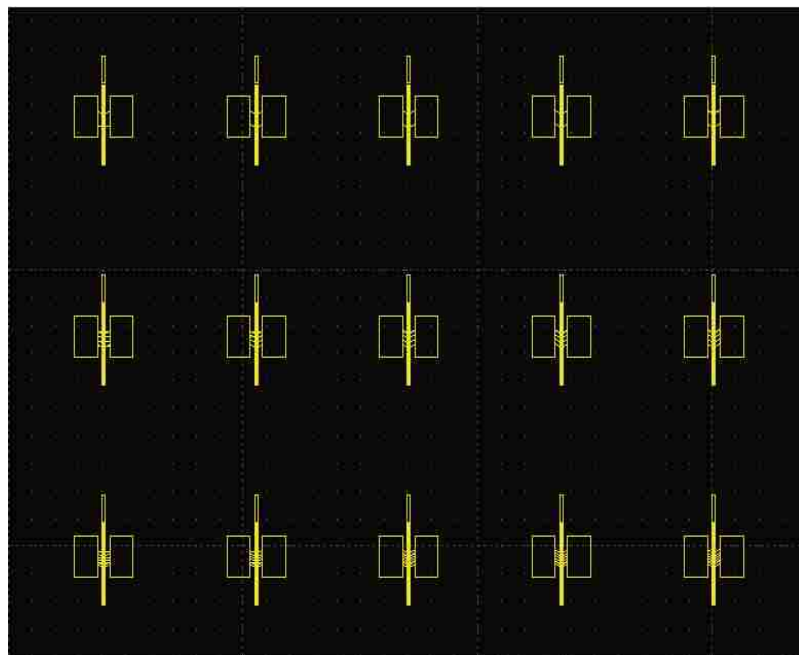


Figure 3.7: Computer Aided Design of Several Devices

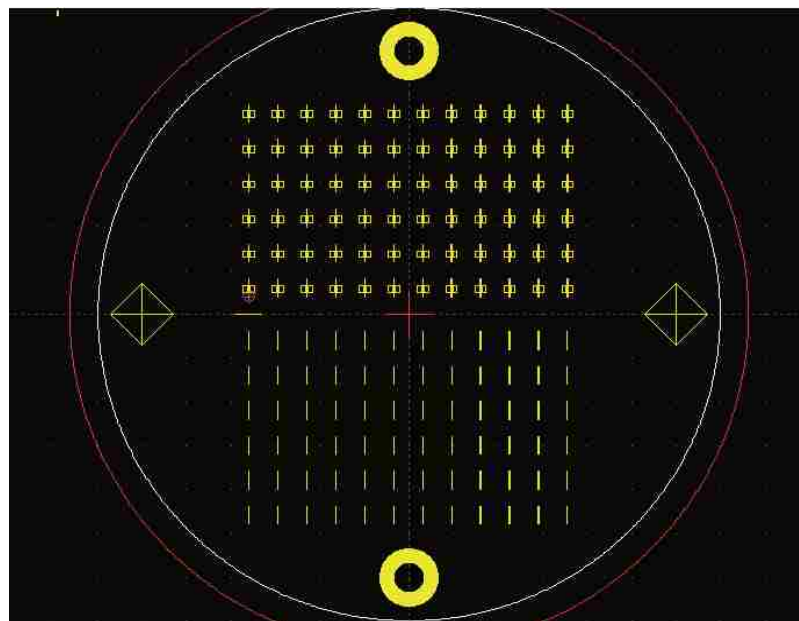


Figure 3.8: Computer Aided Design of Full Mask

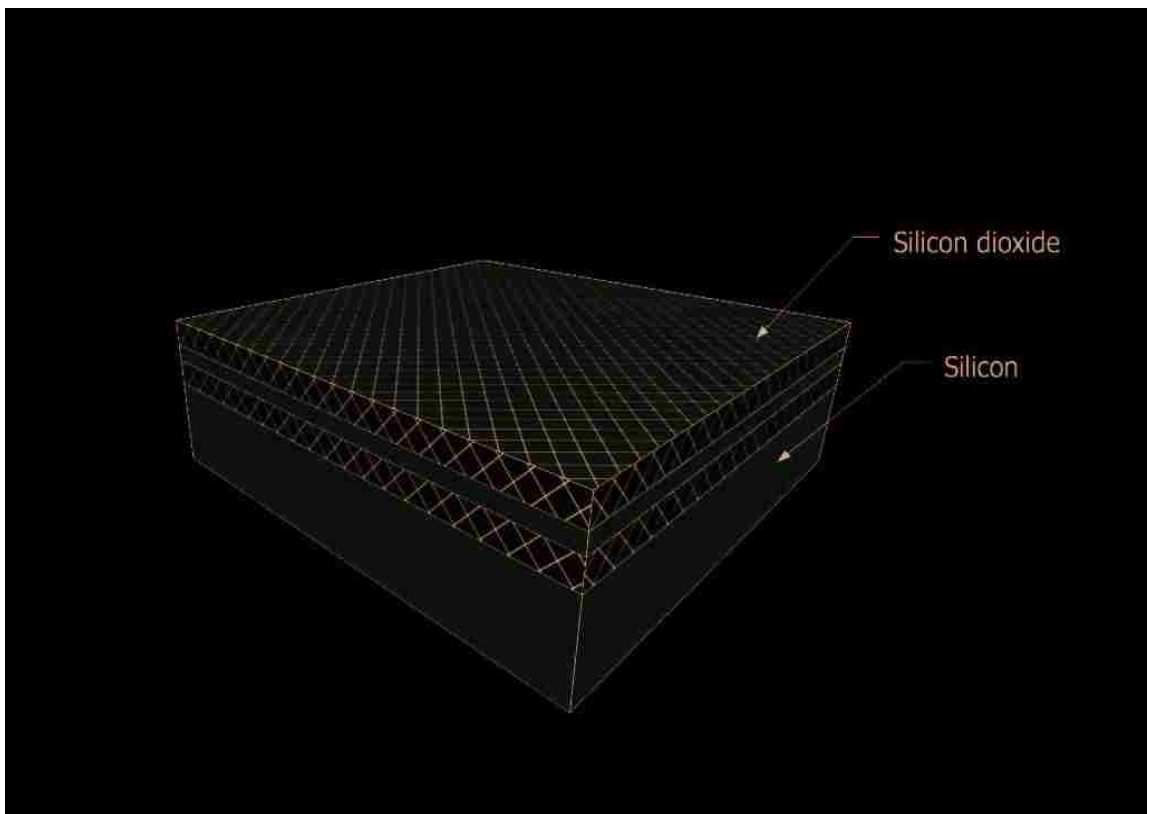


Figure 3.9: Base Material

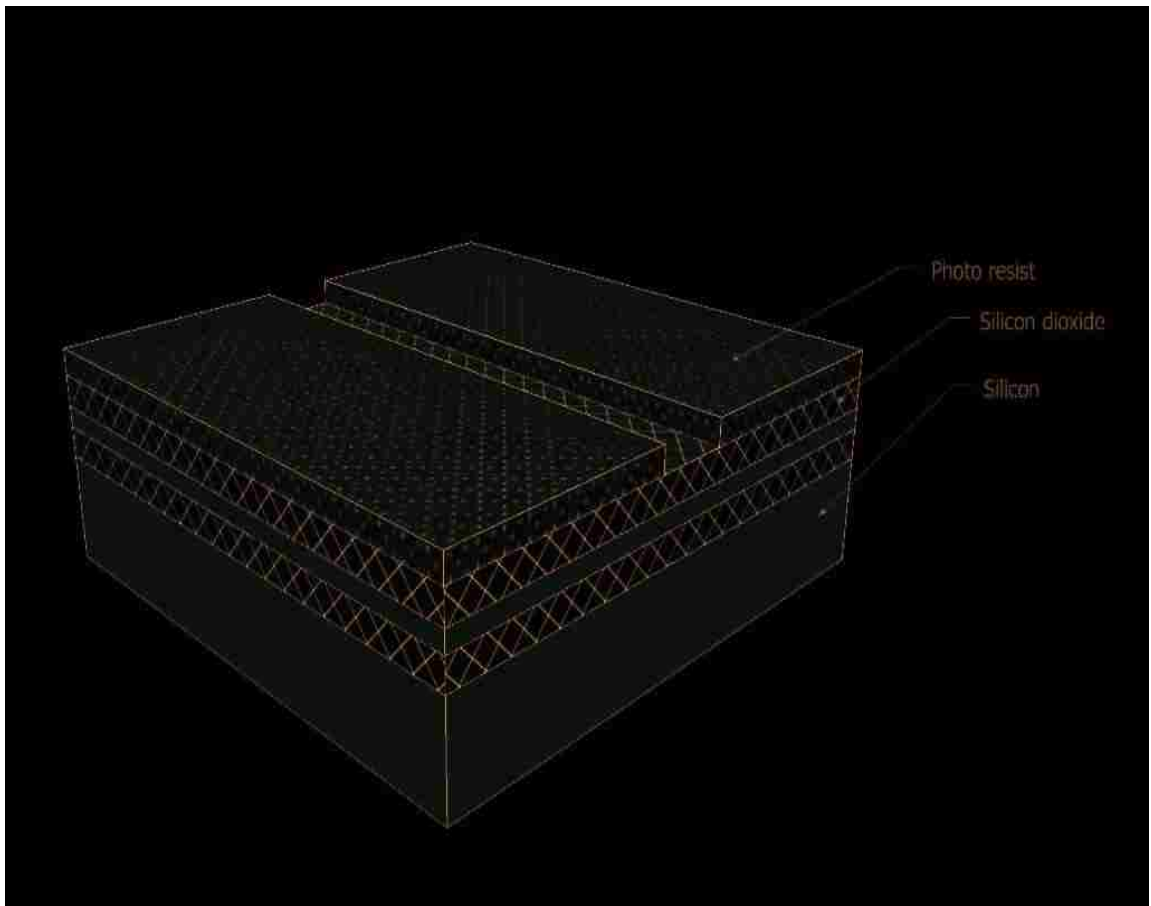


Figure 3.10: Trench Pattern in PR over Silicon Dioxide

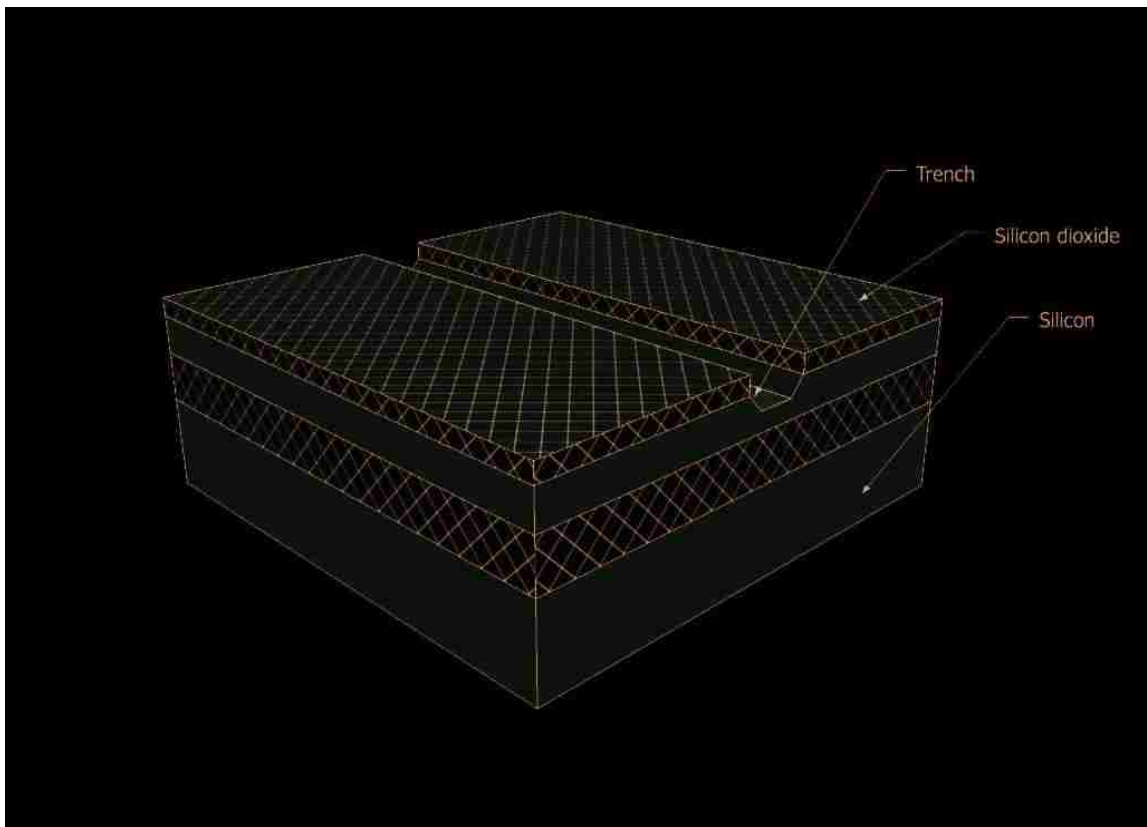


Figure 3.11: Trench Pattern Etched

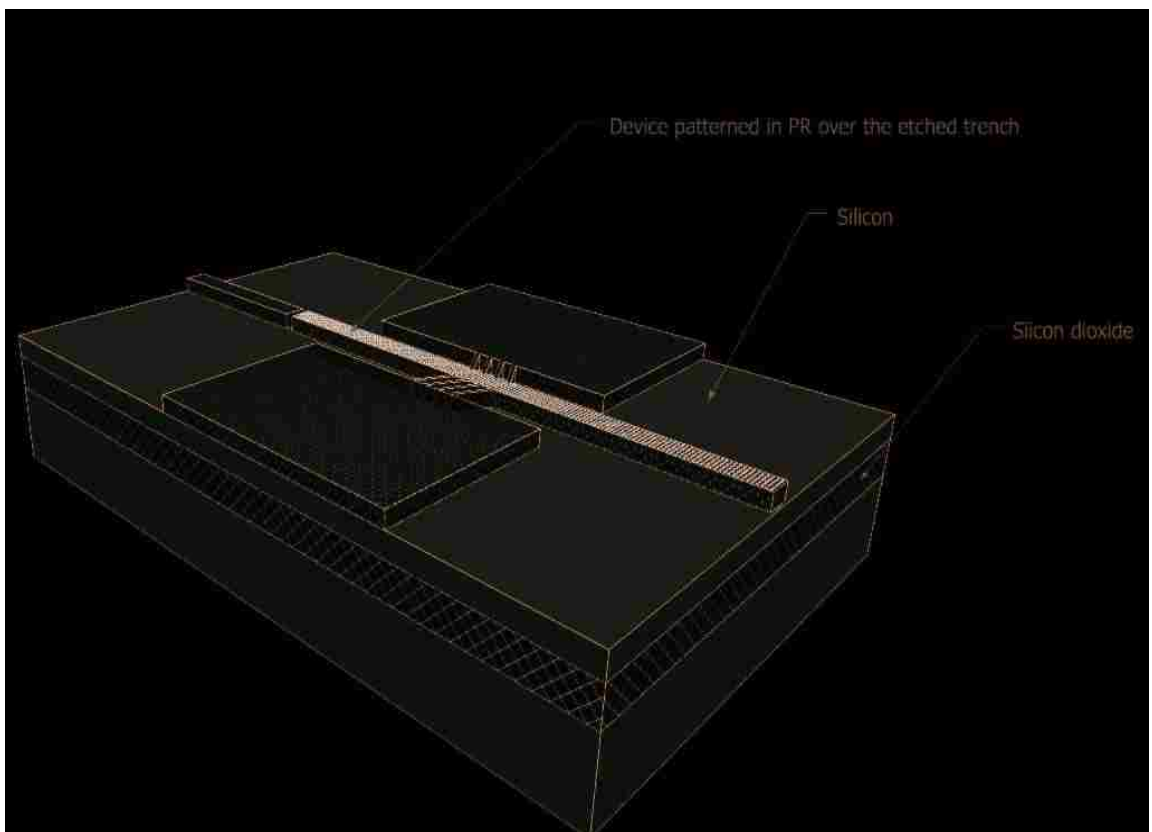


Figure 3.12: Device Pattern over Trench

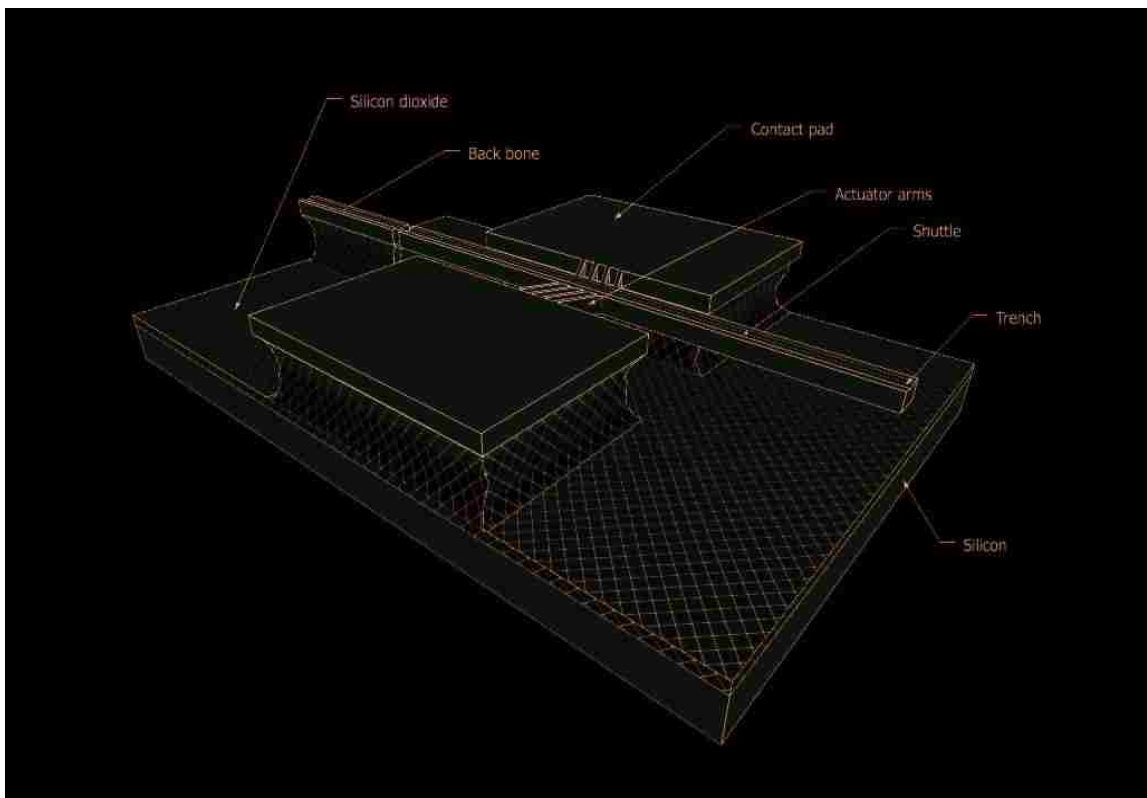


Figure 3.13: Final Device

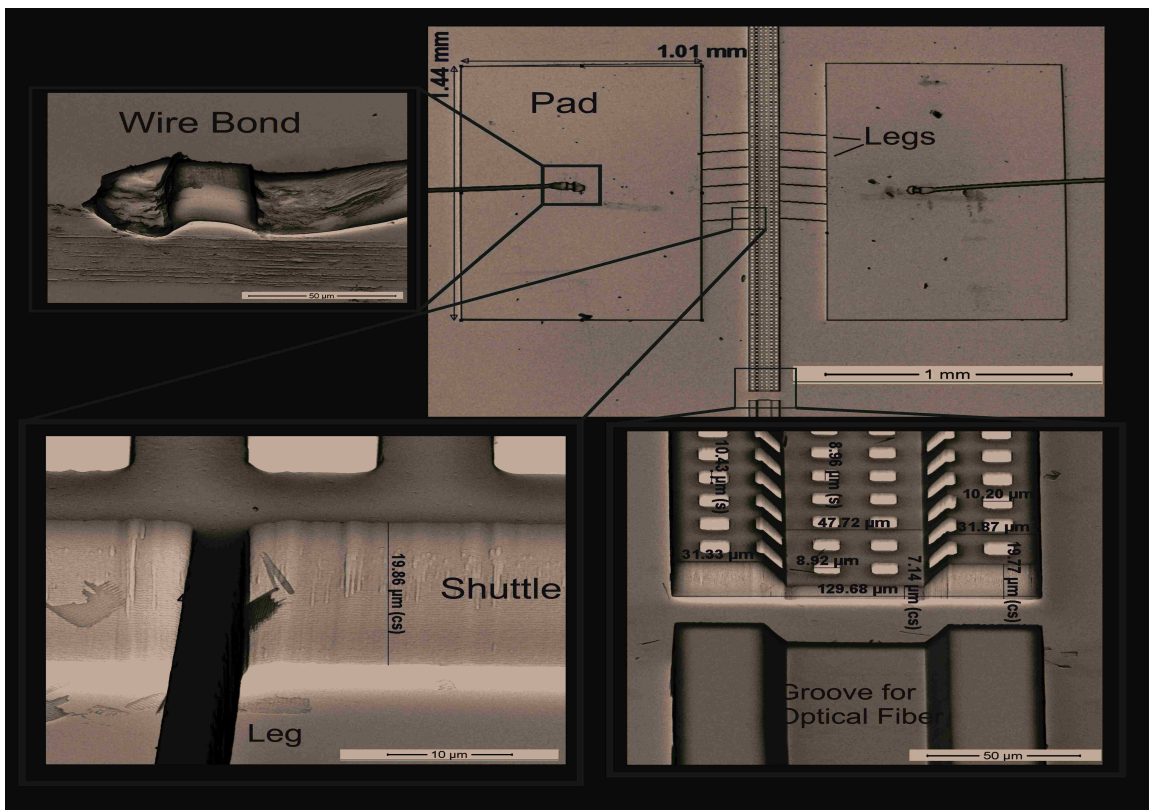


Figure 3.14: Final Device

Chapter 3. Thermal Actuator Fabrication and Characterization

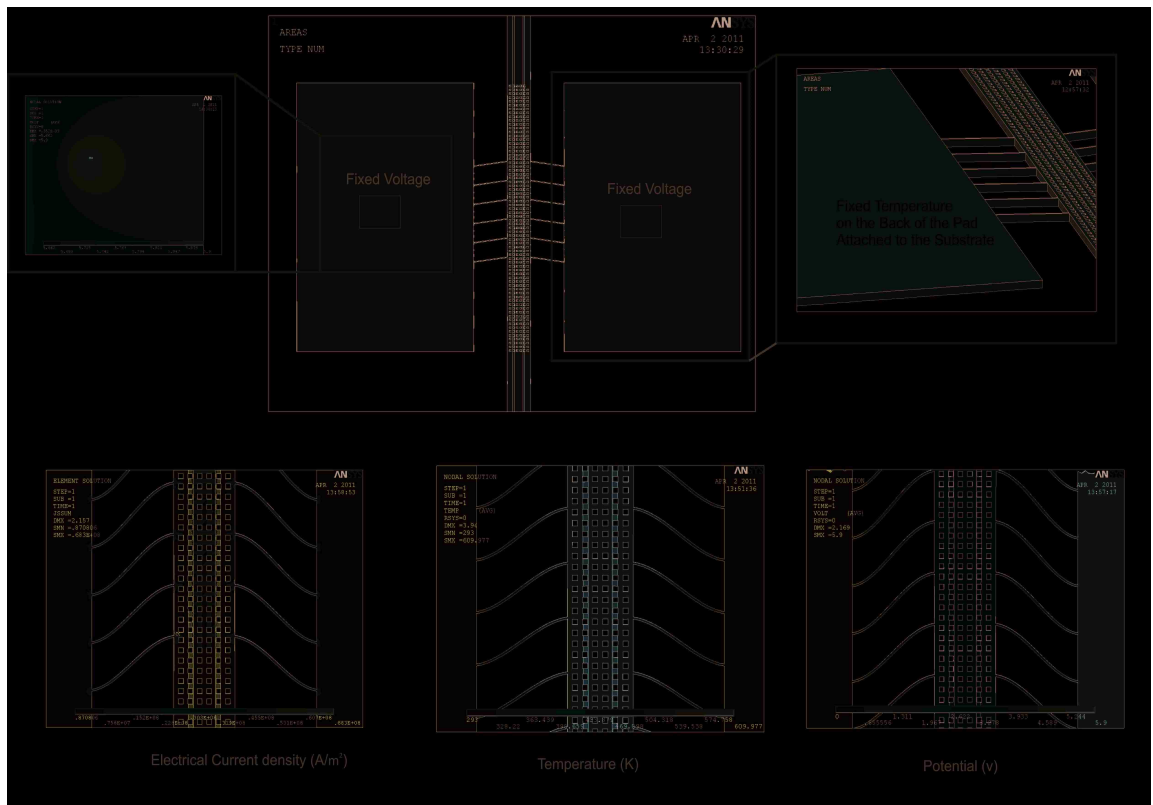


Figure 3.15: ANSYS Simulation Results

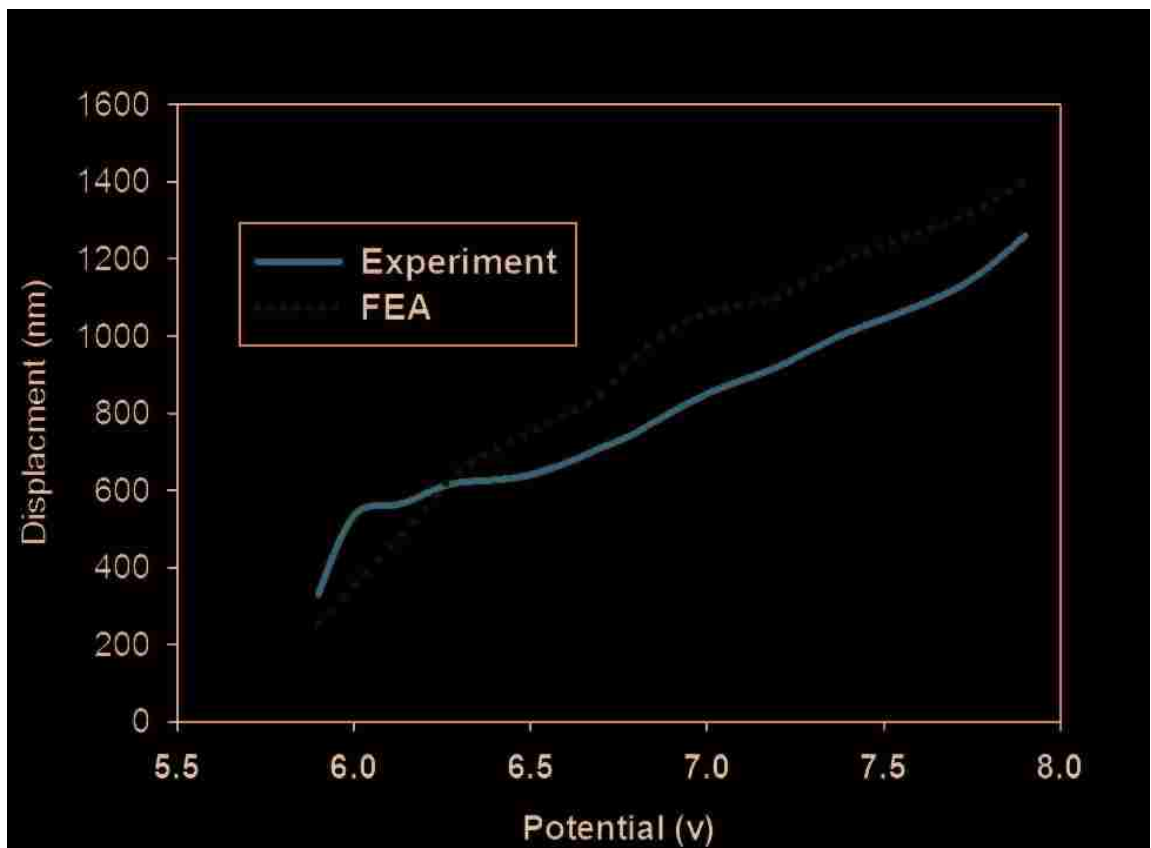


Figure 3.16: ANSYS FEM of thermal actuator in this work

Chapter 4

Cavity Resonators

This section introduces the basic theory essential to understand the confinement of light in Optical Cavity Resonators. It begins with a review of: Gaussian Beams definition and its characteristic parameters, resonators, types of resonators, analysis of resonator stability and the resonant properties of Passive Optical Cavities. At the end of this chapter the Theory of Quantum Atomic Cavities will be outlined. All information in this chapter will be necessary for a complete understanding of the ultra smooth micro mirrors characterization in Chapter 4.

4.1 Cavity Resonators Classical Theory

4.1.1 Gaussian Beam

A Gaussian Beam consists of the electromagnetic radiation of whose transverse electric fields and intensity are described by Gaussian functions. The solution of the Helmholtz equation describes as a Gaussian function represented by the complex amplitude of the electric field, which propagates as an electromagnetic wave in the

Chapter 4. Cavity Resonators

beam.

$$E(r, z) = E_0 \frac{w_0}{w(z)} \exp\left(\frac{-r^2}{w^2(z)}\right) \exp\left(-ikz - ik\frac{r^2}{2R(z)} + i\zeta(z)\right) \quad (4.1)$$

where,

r is the radial distance from the central axis of the beam

z is the axial distance from the beam's waist

k is the wave number $\frac{2\pi}{\lambda}$

E_0 electric field.

λ is the wavelength of the electro magnetic field.

$w(z)$ is the radial distance from the center axis of the beam at which the field amplitude and intensity drop to $1/e$ and $1/e^2$, respectively, of their axial value.

w_0 is the beam's waist size (radius).

From this equation one can find the following beam parameters as seen in Figure 4.1a.

Spot Size $w(z)$ represents the variation of the beam radius along the propagation direction

$$w(z) = w_0 \sqrt{1 + \left(\frac{z}{z_R}\right)^2} \quad (4.2)$$

where the z axis origin is defined to coincide with the beam waist.

Rayleigh Range (z_R) Axial distance from beam waist where the area of the beam x-section is double.

$$z_R = \frac{\pi w_0^2}{\lambda} \quad (4.3)$$

which is called Rayleigh range.

Radius of Curvature of the wavefronts comprising the beam is defined by,

$$R(z) = z \left[1 + \left(\frac{z_R}{z}\right)^2 \right] \quad (4.4)$$

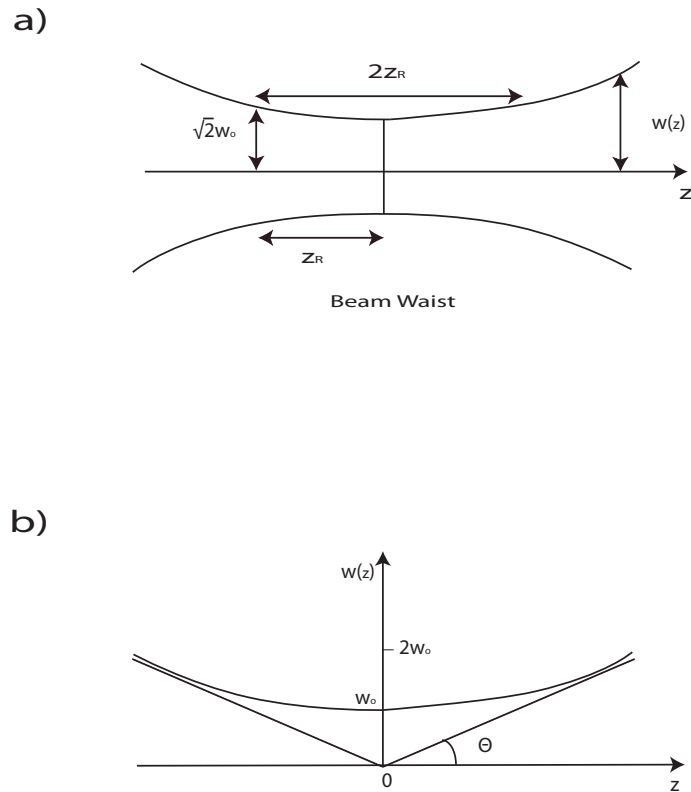


Figure 4.1: Gaussian Beam Parameters

Divergence of the Beam is defined by the angle between the straight line and the central axis of the beam when $z \gg z_R$, see Fig 4.1b:

$$\theta \simeq \frac{\lambda}{\pi w_0} \quad (4.5)$$

4.1.2 Resonator

A resonator is a system or device that shows resonance, that is, it oscillates at some frequencies with a larger amplitude than at others. The resonance frequencies

Chapter 4. Cavity Resonators

of resonators are called normal modes. The light beam travels approximately at a constant velocity, reflecting back and forth between the mirrors of the cavity. Suppose that the length of a cavity is L , then the length of the round trip is $2L$. In order to cause resonance, the light needs to constructively interfere after a round trip, in other words the phase of a wave has to be equal to the initial phase after a round trip. For resonance, the wave has to satisfy the condition that the round trip distance $2L$ is equal to an integer number of wavelength, λ , of the wave.

$$2L = N\lambda, N \in 1, 2, 3, \dots \quad (4.6)$$

When the wave velocity is v , the frequency is equal to $f = \frac{v}{\lambda}$, so the resonance frequencies are:

$$f = \frac{Nv}{2L}, N \in 1, 2, 3, \dots \quad (4.7)$$

4.1.3 Resonator Types

A cavity can be formed by two mirrors facing each other. The simplest type of cavity is formed by two plane parallel mirrors. It is known as Fabry-Perot cavity. Although, it is the simplest, it is not used in large scale lasers due to the difficulty of alignment. They have to be aligned parallel within a few seconds of an arc in order to avoid the walk-off effect. That is, the cavity will spill out light on the extremes of the cavity. In order to avoid the walk-off effect two concave spherical mirrors can be used in place of the two parallel mirrors or the cavity composed by a flat and concave spherical mirror. The radiation pattern will be different for each type of cavity configuration as it is seen in the Figure 4.2. The patterns could be plane-parallel, concentric, confocal, hemispherical, or concave-convex. In the ideal plane parallel configuration the beam travels parallel without suffering any change in its paraxial shape. In the confocal configuration both concave mirrors have the same focal point inside the cavity. Similarly, the concentric configuration both concave mirrors share the

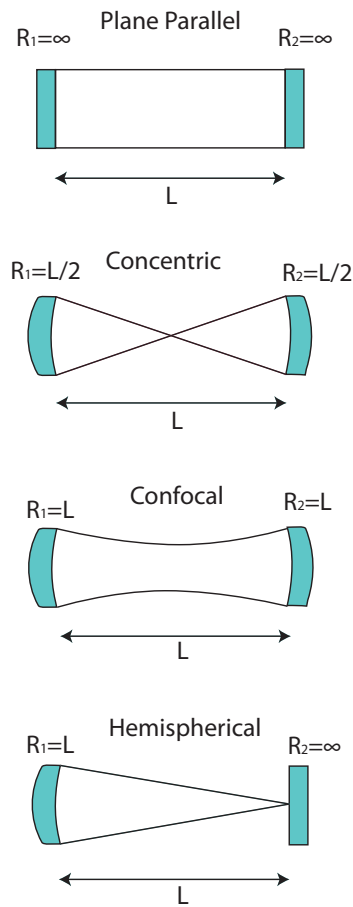


Figure 4.2: Resonator Types

same origin, but the beam waist is minimized. For the hemispherical configuration, formed by a concave and plane mirrors, the focal point is localized at the plane mirror's surface when the radius of curvature of the concave mirror is equal to the cavity length.

4.1.4 Stability

The stability of the resonator is of extreme importance. Stability in this context means the beam size does not grow without limit; instead it is going to be refocused

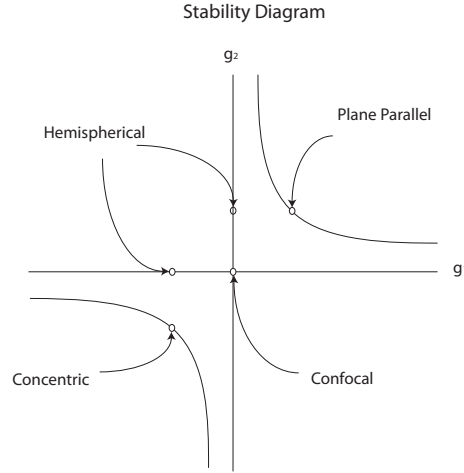


Figure 4.3: Resonators Stability

into the cavity. By using methods such as ray transfer matrix analysis it is possible to calculate a stability criterion in function of the cavity length and curvature mirrors.

$$0 \leq \left(1 - \frac{L}{R_1}\right)\left(1 - \frac{L}{R_2}\right) \leq 1 \quad (4.8)$$

where L is cavity length. The factor $\left(1 - \frac{L}{R_{\#}}\right)$ is termed the stability parameter and is represented by $g_{\#}$

$$0 \leq (g_1)(g_2) \leq 1 \quad (4.9)$$

Relating the Gaussian beam parameters studied above in terms of the g parameters:

$$w_O^2 = \frac{L\lambda}{\pi} \sqrt{\frac{g_1 g_2 (1 - g_1 g_2)}{(g_1 + g_2 - 2g_1 g_2)^2}} \quad (4.10)$$

$$z_R = \frac{g_1 g_2 (1 - g_1 g_2)}{(g_1 + g_2 - 2g_1 g_2)^2} L^2 \quad (4.11)$$

Fig. 4.3 shows the stability diagram given by g_1 and g_2 which represents the axis of the plane. The cavity is stable if the points g_1 and g_2 are positive and limited

by the area formed by the parabola and positive axes, or if the points g_1 and g_2 are negative and limited by the area formed by the parabola and negative axes.

4.1.5 Source of Optical Resonator Loss

There are two main sources of loss in optical resonators:

- (1) inherent losses due to reflectance imperfections at the mirrors and
- (2) losses referable to absorption and scattering in the medium between the mirrors.

The round trip power attenuation factor associated with these processes is defined by $e^{-2\alpha_s d}$, where α is the absorption coefficient of the medium and d is the cavity length. For mirrors of reflectance $R_1 = r_1^2$ and $R_2 = r_2^2$ the wave intensity decreases by the factor $R_1 R_2$ in the course of the two reflections, one in each mirror in a single round trip. Therefore, the intensity attenuation factor is:

$$r^2 = R_1 R_2 e^{-2\alpha_s d} \quad (4.12)$$

where α represents the effective total distributed loss coefficient. Thus,

$$\alpha_{m1} = \frac{1}{2d} \ln\left(\frac{1}{R_1}\right) \quad (4.13)$$

$$\alpha_{m2} = \frac{1}{2d} \ln\left(\frac{1}{R_2}\right) \quad (4.14)$$

are the loss coefficients for the two mirrors. $\ln(\frac{1}{R})$ is termed the δ notation for cavity losses[25].

The transmission intensity through the cavity is given by:

$$I_T = \frac{T_{max} I_{inc}}{1 + \left(\frac{2\mathcal{F}}{\pi}\right)^2 \sin^2\left(\frac{\pi n u}{\nu_{FSR}}\right)} \quad (4.15)$$

From this equation we can find three parameters used to characterize an optical cavity. They are finesse (\mathcal{F}), Free Spectral Range (FSR) and linewidth (κ). The FSR is the frequency of the optical cavity's axial (Gaussian shape) resonator modes.

Chapter 4. Cavity Resonators

The linewidth, is the width (typically the full width at half maximum, FWHM) of its optical spectrum. The finesse, is defined as its FSR divided by the linewidth of its resonances.

The finesse defines the sharpness of the resonance peaks. Assume that we can have an ideal mirror with reflectance close to 1, then the finesse is defined by:

$$\mathcal{F} = \frac{2\pi}{\delta\mathcal{C}} \quad (4.16)$$

The next parameter found in the transmission intensity equation is the free spectral range, which is the frequency spacing between two successive longitudinal modes. It is defined by:

$$\nu_{FSR} = \frac{c}{2L} \quad (4.17)$$

The third basic cavity property is the linewidth, represented by 2κ . Also called sometimes the full-width at half-maximum (FWHM). κ is related to finesse and free spectral range by,

$$\kappa = \frac{\nu_{FSR}}{2\mathcal{F}} \quad (4.18)$$

4.1.6 Resonance Properties of Passive Optical Cavities

Further analysis of an optical cavity yields that only part of the incident signal is reflected of mirror (M_1) Fig 4.4. The portion of the incident light confined in the cavity which is called circulating signal, and the other fraction of the incident light will be transmitted through the second mirror (M_2). The incident, reflected and transmitted signal are capable of being measured, but the circulating or intra-cavity beam cannot be quantified. However, its properties can be inferred from the transmitted and reflected beams. Thus, knowing the properties of the intra-cavity beam are essential in Cavity QED experiments, because the circulating intensity inside the cavity will interact with the confined matter. Analyzing what happens

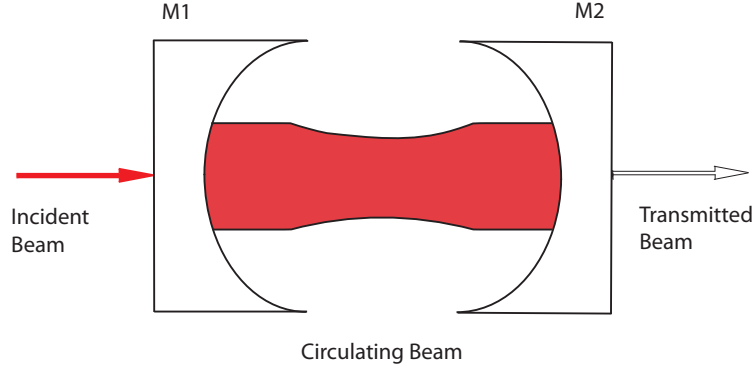


Figure 4.4: Optical Cavity

at input mirror (M_1), the circulating signal E_{cir} consists of the vector sum of that portion of the incident signal which is transmitted through the input mirror (M_1) and has the value of jt_1E_{inc} , plus a contribution representing the circulating signal E_{cir} , which left this same point one round trip earlier and is back to the same point after bouncing-off the second mirror (M_2). So we can express the circulating signal just inside mirror M_1 as:

$$E_{cir} = jt_1E_{inc} + g_{rt}(w)E_{cir} \quad (4.19)$$

where g_{rt} is the net complex round trip gain for a wave making one complete round trip into the intracavity. However, one must consider losses intrinsic to the mirror materials as well. Using α as the voltage absorption coefficient. The signal amplitude causing a round trip signal reduction is $e^{-2\alpha L}$, where L is the length of the cavity. Also, the signal will suffer a phase shift represented by $e^{\frac{jwL}{c}}$. After considering these loss factors, one can represent the complex round trip gain as:

$$g_{rt}(w) \cong r_1r_2e^{\alpha_o L - \frac{jwL}{c}} \quad (4.20)$$

The round trip gain will be less than unity. The phase accumulated by the circulating field traveling a distance $2L$ is ϕ . This phase is given by:

$$\phi = 2kL = 2\pi\nu\frac{2L}{c} = 2\pi\frac{\nu}{\nu_{FSR}} \quad (4.21)$$

Chapter 4. Cavity Resonators

From above equation we can find the factor $\frac{E_{cir}}{E_{inc}}$

$$\frac{E_{cir}}{E_{inc}} = \frac{it_1}{1 - r_1 r_2 e^{\frac{-i2\pi\nu}{\nu_{FSR}}}} \quad (4.22)$$

Using a similar analysis done in input mirror (M_1) at the second mirror(M_2), one can find the transmitted signal intensity coming out in function of the circulating signal.

$$\frac{E_{cir}}{E_T} = \frac{1}{it_2 e^{\frac{-i4\pi\nu}{\nu_{FSR}}}} \quad (4.23)$$

The intensity of the fields are proportional to the square of the electric field. Therefore:

$$\frac{I_T}{I_{inc}} = \frac{(t_1 t_2)^2}{(1 - (r_1 r_2)^2) \left(1 + \frac{4r_1 r_2 \sin^2\left(\frac{\pi\nu}{\nu_{FSR}}\right)}{1 - (r_1 r_2)^2}\right)} \quad (4.24)$$

$$\frac{I_{cir}}{I_{inc}} = \frac{t_1^2}{|1 - g_r t(w)|^2} \quad (4.25)$$

4.2 Cavity QED System

In this section mathematical details will not be shown. However, the concepts of Cavity QED theory are going to be outlined, as well as important considerations for building a cavity QED that would be useful for quantum information, measurement and control.

4.2.1 Light and Atom Interaction

Quantum Electrodynamics is a branch of atomic physics that studies the interaction of the matter with quantized electromagnetic fields[9]. Haroche and Raimond [10]demonstrated a model for atoms and photons which is a mechanical analogy to

Chapter 4. Cavity Resonators

springs in the case of the field oscillation and spins for the case of the two atom system. In physics the representation of atoms as two level states is often a good approximation. Hence, when an atom interacts with a field oscillator at resonance with an atomic transition, between two non-degenerate energy states it is justifiable to ignore all the other levels and work with a two states model. Note that the spring models are designed to represent systems which are able to give and receive quanta energy.

The model for an electromagnetic field is usually described as a group of independent oscillators. Therefore, cavity QED can be defined as the physics of a system formed by a spring and an oscillator in interacting. Mainly in cavity QED, the goal is to achieve an atom's isolation in a cavity which is formed with highly reflecting mirrors. The electric field is quantized into the cavity as set of quantum harmonic oscillators, one of them being resonant with a transition between two levels of the atom which thus behaves as a spin. The field oscillator cannot be considered independent of the cavity mirrors which define the mode structure. This implies that the atom is directly interacting with a macroscopic object, the cavity which surrounds it.

Jaynes and Cummings [15] developed a theoretical model to describe the system of a two-level atom interacting with a quantized mode of an optical cavity. The spin-oscillator Hamiltonian that describe the full system consist of the free field Hamiltonian, the atomic excitation Hamiltonian and the Jaynes-Cummings interaction Hamiltonian.

$$\hat{H}_{\text{JC}} = \hat{H}_{\text{field}} + \hat{H}_{\text{atom}} + \hat{H}_{\text{int}} \quad (4.26)$$

Each term expanded:

$$\hat{H}_{\text{JC}} = \hbar\nu\hat{a}^\dagger\hat{a} + \hbar\omega\frac{\hat{\sigma}_z}{2} + \frac{\hbar\Omega}{2}(\hat{a}\hat{\sigma}_+ + \hat{a}^\dagger\hat{\sigma}_-) \quad (4.27)$$

where the operators $(\hat{\sigma}_z, \hat{\sigma}_+, \hat{\sigma}_-)$ are the Pauli operators for inversion, raising and lowering of the atomic state, while $(\hat{a}^\dagger, \hat{a})$ are the creation and annihilation operators for the photons in the coupled mode resonator, (ω, ω_2) are the resonant frequencies of the atom and cavity[19]. The Jaynes-Cummings interaction Hamiltonian is the scalar product of the atomic dipole operator and the cavity electric field operator at the atomic location. The solution of this scalar product is reduced to a function formed by the difference between annihilation operator times raising operator and creation operator times lowering operator of the atom all this multiplied by the Rabi frequency(Ω). The Rabi frequency gives the strength of the coupling between the light and the transition given an atomic transition in a given light field.

4.3 Strong Coupling for Open Quantum Systems

The cavity QED depicted in Fig. 4.4 is for system formed by a pair of mirrors which form an open cavity where an intracavity field is generated. The intracavity field has a decay rate represented by κ . Inside the cavity a two-state atom with an atomic decay rate, represented by γ , will interact with the quantized field, and the coupling frequency of the two-state atom to the cavity mode is represented by g^1 . The aim of this work is provide a tool to comply with the considerations proposed by H.R.Kimble [7] for investigation of quantum dynamical processes for a small collection of atoms strongly coupled to intracavity field of a very high finesse optical cavity. This must occur in a regime for which the time scale for coherent, reversible evolution is comparable with that for irreversible decay by way of atomic spontaneous emission and of loss through the cavity mirrors. Quantitatively the means to achieve this situation is:

$$g \gg (\gamma, \kappa) \tag{4.28}$$

¹Not to be confused with the laser stability parameter g described in Section 3.1.4

Chapter 4. Cavity Resonators

which is known as the strong coupling regime. In this state, the number of photons required to saturate an intracavity atom is $n_0 \sim \frac{\gamma^2}{g^2} \leq 1$, and the number of atoms required to have an appreciable effect on the cavity field is $N_0 \sim \frac{\kappa\gamma}{g^2} < 1$.

The coherent coupling between the l th atom and the cavity mode is $g(\vec{r}_l)$ with

$$g(\vec{r}_l) = \left(\frac{\mu^2 \omega_C}{2\hbar \epsilon_0 V_m} \right)^2 \psi(\vec{r}_l) \equiv g_0 \psi(\vec{r}_l) \quad (4.29)$$

Where the cavity mode function is spatially dependent due to the Gaussian standing wave of the Fabry-Perot cavity electric field. $\psi(\vec{r})$ is given by:

$$\psi(\vec{r}) = \cos(kx) e^{-\frac{(y^2+z^2)}{\omega_o^2}} \quad (4.30)$$

So the volume of the electric field mode V_m is:

$$V_m = \int |\psi(\vec{r})|^2 d\vec{r} = \frac{\pi}{4} \omega_o^2 L \quad (4.31)$$

These equations show that coherent coupling between an atom and cavity field is inversely proportional to the cavity mode volume. If we want to obtain a large rate g value, one must reduce the cavity mode volume by reducing the cavity length, which is proportional to the cavity volume. This is the justification by which this project was undertaken to create micro cavities with MEMS for cQED.

Chapter 5

Micro Cavity Characterization

In this chapter, the characterization result of the micro mirrors is presented. It starts with a detailed explanation of the experimental setup followed by the results and analysis of the micro mirror characterization.

5.1 Experimental Setup

An infrared laser, Sanyo model DL7140-201S, was used as light source. Its wavelength was set to 780 nm with a threshold current equal to 30 mA and an operating current of 135 mA for a power of approximately 70 mW. The radiation was coupled to a single mode polarization maintaining optical fiber, to deliver the light into the cavity. Mode matching optics are necessary to shape and focus the input the beam and match an elliptical Gaussian mode to the circular Gaussian mode of the fiber. The mode matching optics consist of a pair of collimating lenses, a pair of $\frac{\lambda}{2}$ waveplates, an optical isolator, a pair of high reflectance mirrors and a fiber coupler. Figure 5.1 shows the optical configuration to mode match and couple the laser light to the optical fiber.

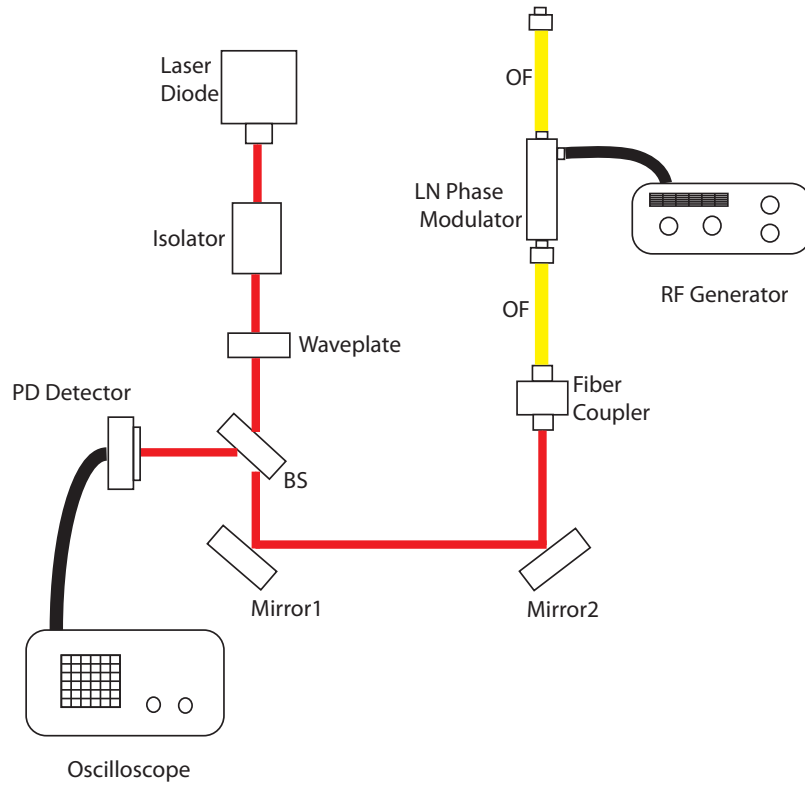


Figure 5.1: Mode Matching Setup

The light was aligned through the optical path to the fiber coupler. Plugging a laser in the input port and a laser in the output port, allows for verification of the optical path alignment, because both beams must overlap. Once verified the beam size is adjusted using the collimation lenses located in the laser source mount and in the fiber coupler until the maximum output is observed in the photodetector (EOT Silicon PIN Detector ET2030). A coupling efficiency of approximately 75% was readily obtained with this setup.

The output of the mode matching optics was connected to a Lithium Niobate(LN) phase modulator (Photline Technologies Model NIR MPX800). When a voltage is applied to the RF electrode of the phase modulator, one wave is added, which means

Chapter 5. Micro Cavity Characterization

$n + 1$ waves exist in the same length. The phase modulator helps us to calibrate the measurements in terms of optical frequency.

A second section train of optics brings the light to the optical cavity. It is used to point the reflected light from the cavity to the photodetector. This section of optics consist of a pair of collimating lenses, a polarized beam splitter cube, a beam splitter and $\frac{\lambda}{2}$ waveplate. The set up is shown in the figure 5.1.

A half symmetric cavity formed of a flat and concaved mirror was built. The micro mirrors were fabricated using chemical wet etching and smoothed with multiple oxidation smoothing cycles that created a surface roughness of 2.2 \AA as confirmed by AFM measurement as is indicated in Fig. 5.2.

A flat mirror on BK7 substrate and the micro-mirrors, were coated via an ion beam sputtering technique with a dielectric mirror stack consisting of SiO_2 and Ta_2O_5 layers to gives a maximum reflectivity of 99.99% for 780nm laser wavelength. Both mirrors were attach to a frame that keep them aligned perpendicularly one to each other. Piezo benders (Physik Instrumente PL0XX) were attached behind the micro mirror substrate for adjusment of the spacing between it and the flat mirror.

The testing equipment was arranged as follows: The photodetector was connected to the oscilloscope (Tektronix TDS2004B - 60MHz) to measure the reflection signal from the cavity. In order to control the piezo bender, a frequency generator(HP Pulse Generator 8111A) was connected to a low noise pre amplifier (Stanford Research Systems Model: SR 560) which helped to reduce the noise and improve the repeatability of the piezo oscillations and displacement. A piezo controlled (Physik Instrumente E-500) was connect between the pre amplifier and piezo bender to amplify the function generator signal. Finally, a RF Generator was used to generate the signal for the LN phase modulator.

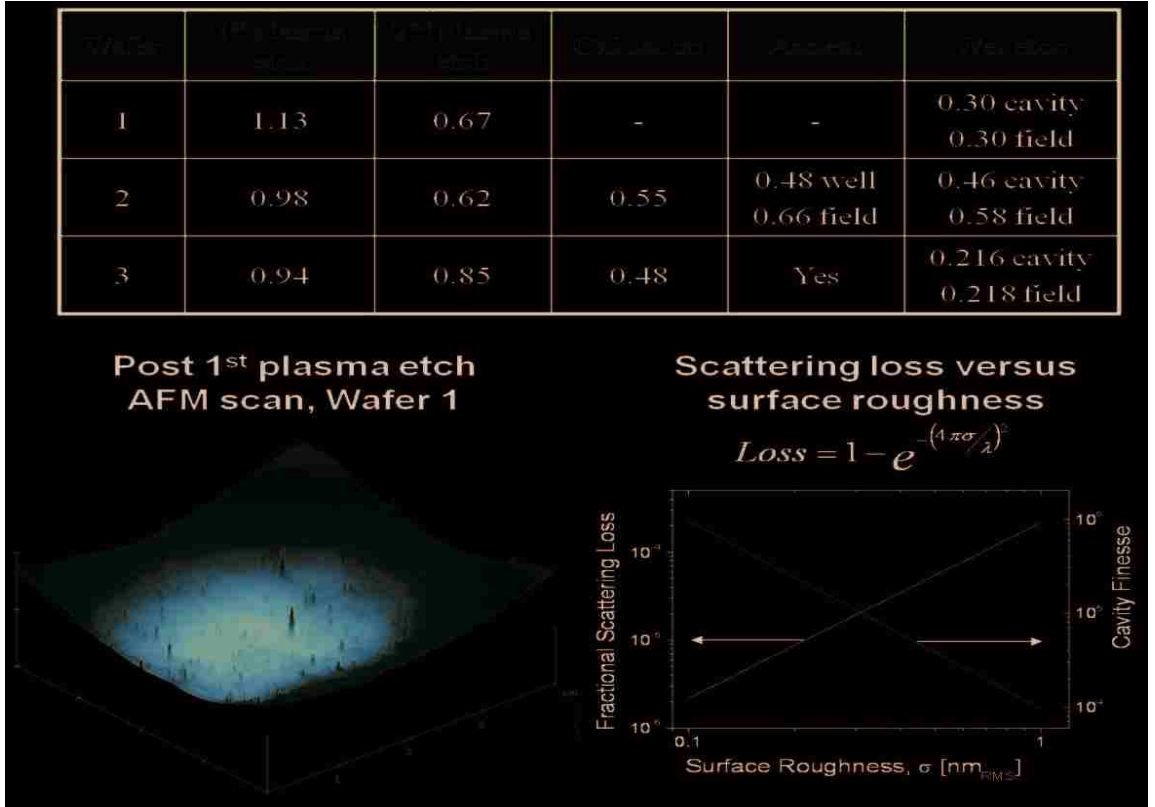


Figure 5.2: Surface Roughness

5.2 Experiment Results

The efficiency for an atom cavity system is described by the single atom cooperativity [8]

$$C_1 \equiv \frac{g_o^2}{\kappa\gamma} \quad (5.1)$$

C_1 is the inverse of the critical atom number N_o , which describes how many atoms are required to affect the cavity field. The strong coupling regime is required to have a C_1 larger than unity. One way to maximize C_1 is to increase the cavity finesse, \mathcal{F} , since

$$\kappa \approx \frac{\pi c}{2L\mathcal{F}} \quad (5.2)$$

where L is the cavity length and c is the speed of light. Moreover, the finesse depends on the reflectivity of the cavity mirrors, ρ

$$\mathcal{F} = \frac{\pi \sqrt[4]{\rho_1 \rho_2}}{(1 - \rho_1 \rho_2)} \quad (5.3)$$

because the reflectivity depends on the surface roughness, it is necessary to optimize the smoothness resulting from the mirror fabrication process.

The reflectivity limit due to surface roughness is quantified by the scattering factor:

$$SF = e^{-(\frac{4\pi\sigma}{\lambda})^2} \quad (5.4)$$

where σ is the roughness of the mirror surface and λ is the wavelength of the light. Hence, if the surface roughness in silicon is measured to be 2 nm rms, thereby the finesse of the microcavity will be limited to $\mathcal{F}=6000$.

Micro mirrors were fabricated employing fluorine radicals etching through lithography technique, which define circular apertures in a silicon oxide hard mask to form the micro mirrors in silicon substrate wafer. Once the concave cavities were formed the silicon oxide hard mask was removed. Then, these micro mirrors were smoothed first using an inductively coupled plasma etch with sulfur hexafluoride (SF_6), followed by multiple oxidation smoothing cycles, as is shown in Fig.5.3.

Geometric characterization of the micro mirror was performed using a scanning electron microscope image in the cross section of a micro mirror as is shown in Fig.5.4. The mirror in figure has a depth of 9.75 μm and a chord of 70.5 μm , indicating a radius of curvature (RoC) of 68.6 μm . However, cavity measurements exhibit that the RoC is in fact 251 μm in the region defining the cavity mode. This discrepancy suggested that the micro mirror is aspheric with a slightly flattened bottom. This result is believed to be principally from a small anisotropic component during the initial etching of the cavity using fluorine radicals.

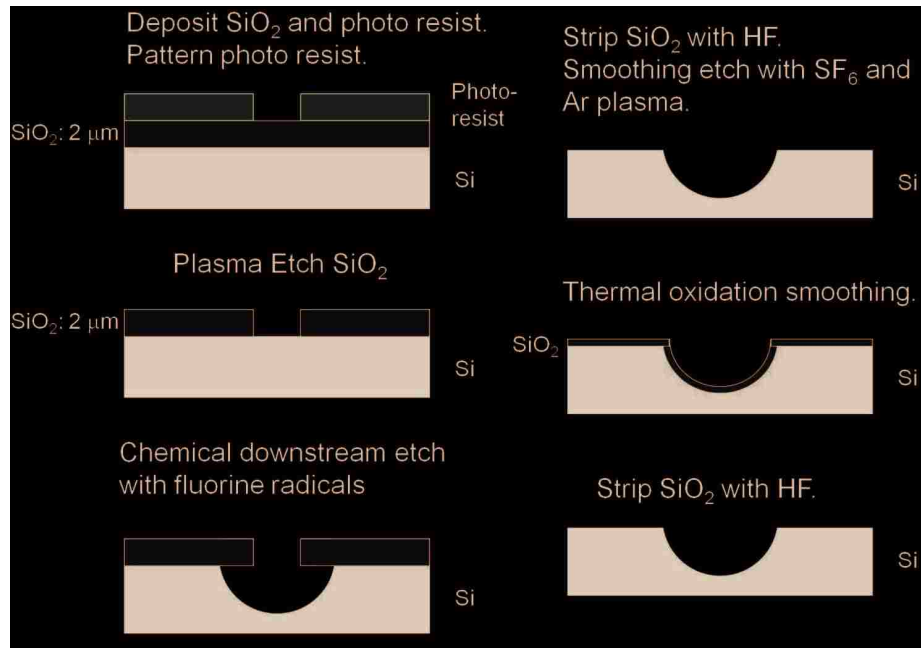


Figure 5.3: Mirror Fabrication Process

The characterization of the mirror's surface roughness after smoothed was performed by acquiring AFM images at the center of the cavity, found by turning off

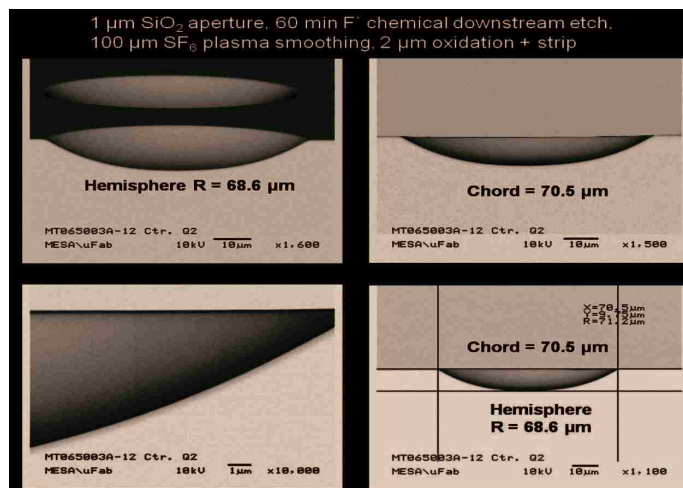


Figure 5.4: Geometric Characterization

real-time background subtraction, and restricting image processing to a linear background subtraction. The post-smoothing roughness of 2.2 \AA rms supports in the best case a reflectivity of 99.9988% and a cavity finesse of $\mathcal{F}=260000$ if the second mirror has equal performance.

To maximize the mirror performance after the surface roughness smoothed, they were coated with a stack of layers consisting of SiO_2 and Ta_2O_5 layers. After coating, the surface roughness increase slight to a 2.6 \AA rms roughness. The optical properties were measure using the experiment set up described in the previous chapter and shown in the Figures 5.2 and 5.3. The cavity is enclosed between the flat mirror and the concave micro mirror and put them together in the frame. The light from the 780nm diode laser is coupled to the cavity through the flat mirror, then a non polarizing beam splitter redirects a portion of the light reflected from the cavity to the fast photodiode. The cavity length was scanned, using the piezo actuators attached to the micromirror substrate.

The piezo amplifier only delivers positive voltage to the piezo bender. This causes the piezo to bend in only one direction, limiting the cavity length scan. However, to overcome this issue, the piezo amplifier was connected in reverse polarity from the previous setup. This allows further extending of the cavity length. The experiment was designed to analyze the cavity parameters for different cavity lengths. Although, the cavity length cannot be measured directly, it can be infered from the FSR. The FSR, Transverse Mode Spacing (TMS), and the FWHM, were measured directly from the oscilloscope. To infer the cavity length and radii of curvature of the micro mirror, the cavity length scan was calibrated in terms of optical frequency. This was accomplished with the addition of 2 GHz sidebands to the light with the fiber-based LN phase modulator.

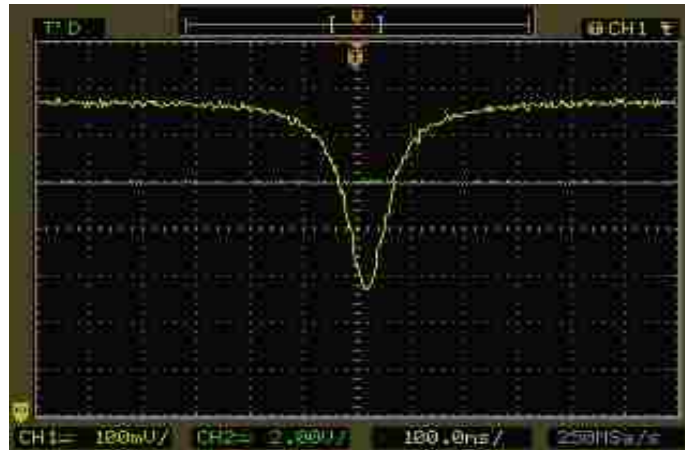


Figure 5.5: Cavity Linewidth

In order to scan the cavity length, the piezo amplifier voltage was adjusted starting from 30 Volts to 0 Volts in steps of 5 Volts. To determine repeatability, multiple measurements of FSR, TMS and FWHM for cavity length were performed. Then, the polarity of the amplifier voltage was reversed on the piezo bender in order to extend the cavity scan. Results are shown in the Fig. 5.5. The cavity length was scanned from $19 \mu\text{m}$ to $123 \mu\text{m}$, with a maximum \mathcal{F} of 64000 at $58 \mu\text{m}$. The RoC is

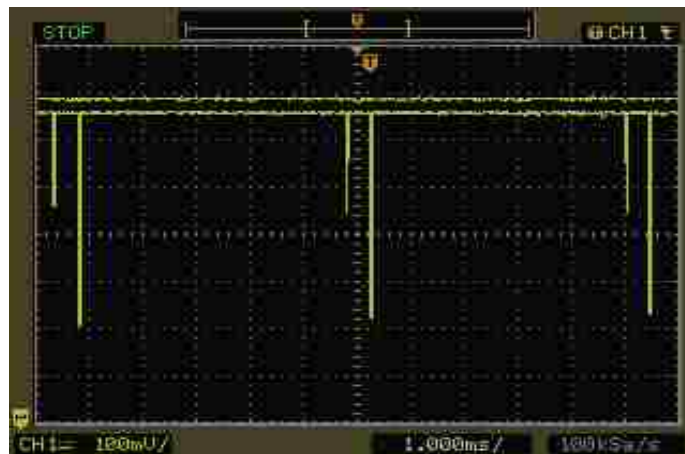


Figure 5.6: Free Spectral Range of the cavity

VDC(volts)	19.6	15	10.2	5.2	0	0	5.2	10.2	15	19.6	25.04	28.12	30.6
Finesse	5.655E+04	5.670E+04	5.832E+04	5.271E+04	5.379E+04	5.323E+04	5.729E+04	6.124E+04	6.407E+04	6.308E+04	5.854E+04	5.937E+04	5.684E+04
L(meters)	1.228E-04	1.111E-04	1.070E-04	9.21222E-05	8.31731E-05	8.47633E-05	7.73299E-05	6.80636E-05	5.80508E-05	4.65084E-05	3.38542E-05	2.49666E-05	1.97917E-05
RoC	2.365E-04	2.335E-04	2.887E-04	2.409E-04	2.655E-04	2.627E-04	2.396E-04	2.460E-04	2.640E-04	2.395E-04	2.412E-04	2.669E-04	2.406E-04
Q	1.781E+07	1.615E+07	1.600E+07	1.245E+07	1.147E+07	1.157E+07	1.136E+07	1.069E+07	9.537E+06	7.523E+06	5.081E+06	3.800E+06	2.885E+06
C1	1.135E+02	1.153E+02	9.921E+01	1.068E+02	1.036E+02	1.028E+02	1.213E+02	1.320E+02	1.390E+02	1.579E+02	1.657E+02	1.811E+02	2.039E+02

Figure 5.7: Parameters Characterization

determined through the spacing of TEM_{00} and TEM_{10} modes.

$$\Delta\nu = \frac{c}{2\pi L} \cos^{-1} \sqrt{1 - L/R} \quad (5.5)$$

RoC within the interacting region of the mirror with the cavity mode is independent of cavity length at the level of $251\mu\text{m}$.

In the Fig. 5.6 shows the RoC calculated for cavity length range from $19\mu\text{m}$ to $123\mu\text{m}$. Moreover, this figure displays the propagation of uncertainty caused during the variables measurement, which are propagated in the function of RoC as:

$$\sigma_{RoC} = \sqrt{\left(\frac{\partial RoC}{\partial L} \sigma_L\right)^2 + \left(\frac{\partial RoC}{\partial FSR} \sigma_{FSR}\right)^2 + \left(\frac{\partial RoC}{\partial TMS} \sigma_{TMS}\right)^2} \quad (5.6)$$

Equation 4.6. describes the errors or uncertainties of cavity length, free spectral range and transverse mode spacing measured. The RoC calculated value was verified with a profile measurement of an identical mirror using a scanning white light interferometer. Fig. 5.7 shows the having a maximum value of 64000 for a cavity length of $58\mu\text{m}$.

Figure 5.8 shows the calculated value of the single atom cooperativity, C_1 , as a function of cavity length, which varies from 99 for the longest cavity to 204 for the shortest cavity ($L=19\mu\text{m}$), indicating that these cavities should exhibit a clear response to the presence of a single atom.

Chapter 5. Micro Cavity Characterization

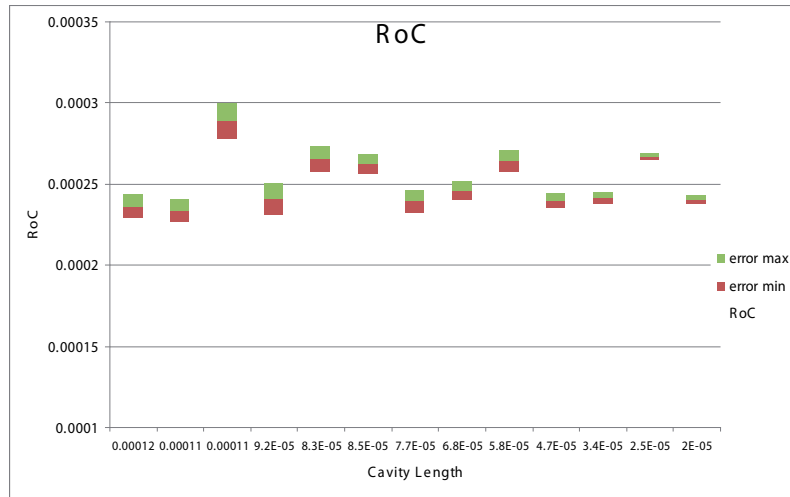


Figure 5.8: Radius of Curvature of the micro-mirrors

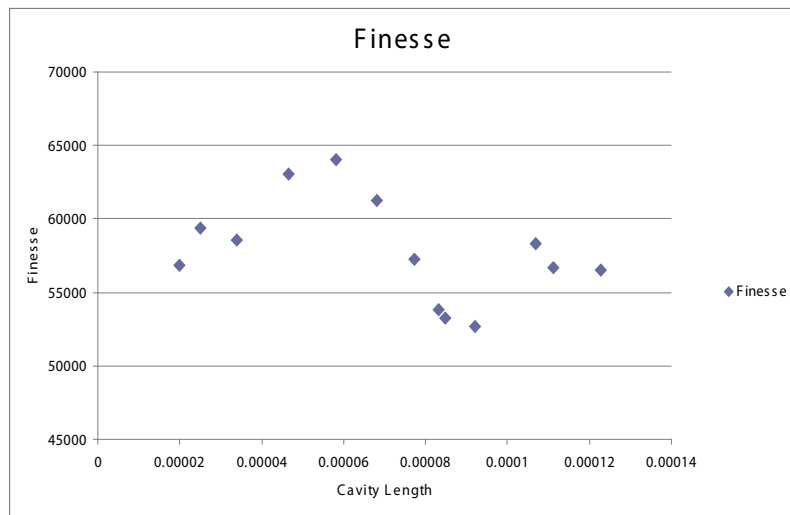


Figure 5.9: Finesse

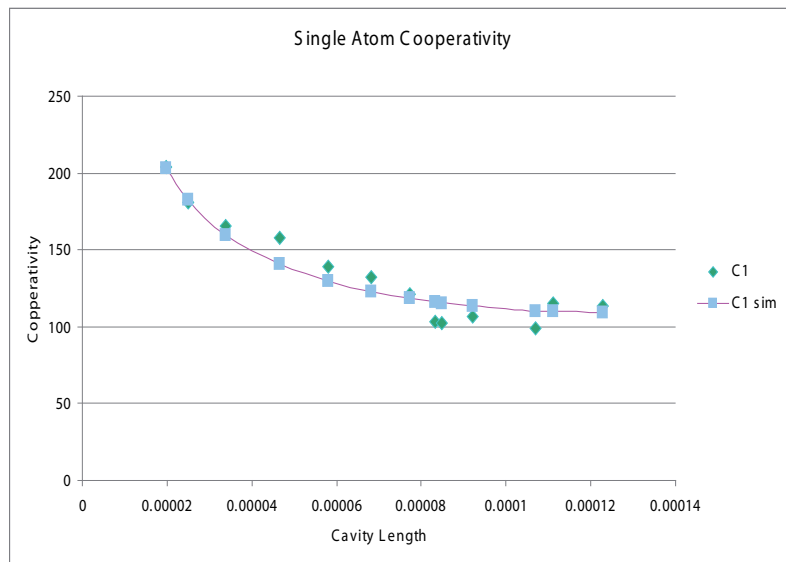


Figure 5.10: Single Atom Cooperativity

Chapter 6

Conclusions

The goal of this thesis was to characterize a micro mirror fabricated in a silicon slab with high reflective coating and build a feasible micro thermal actuator capable to pull a fiber cable for cavity length control. An introduction of the micro thermal actuator and cavity resonator theoretical background was given in order to understand the results of the micro mirrors' characterization and actuator design.

This was followed by a description of the characterization method for the micro mirrors. The micro mirrors were fabricated on a silicon slab with a surface roughness of 2.6 \AA rms. The radii of curvature measured was of $251 \mu\text{m}$, and the expected RoC was of $68.8 \mu\text{m}$. This discrepancy should indicate that the micro mirror is not round and the fabrication is flat at the bottom of the mirror. It was observed that a maximum cavity finesse of 60,000 for a cavity length of $58 \mu\text{m}$, and a single atom cooperativity of 204 for a cavity length of $19 \mu\text{m}$.

A micro thermal actuator was built using standard MEMS fabrication procedure. The actuators have a chevron shape with a middle shuttle where a fiber cable was

Chapter 6. Conclusions

attached. Actuators with different number of mobile arms were fabricated to test the pulling force.

In a future work these two separate devices, the micro mirror and the actuator, will need to be integrated to demonstrate the device actuation and cavity stability. Once this new apparatus is set up in a more integrated system into a vacuum chamber, atoms will be added inside the cavity to realize light-matter experiments.

References

- [1] nobelprize.org/nobel_prizes/physics/laureates/1997/illpres/illpres.html.
- [2] nobelprize.org/nobel_prizes/physics/laureates/1989/illpres/illpres.html.
- [3] <http://www.mems-exchange.org/MEMS/what-is.html>.
- [4] <http://www.el-cat.com/silicon-properties.htm>.
- [5] M.S. Baker, R.A. Plass, T.J. Headley, and J.A. Walraven, *Final Report: Compliant Thermo-Mechanical MEMS Actuators*, Technical Report SAND2004-6635, Sandia National Labs., Albuquerque, NM (US); Sandia National Labs., Livermore, CA (US), 2004.
- [6] D J Bell, T J Lu, N A Fleck, and S M Spearing, *MEMS actuators and sensors: Observations on their performance and selection for purpose*, Journal of Micromechanics and Microengineering **15** (2005).
- [7] P.R. Berman, *Cavity quantum electrodynamics / structure and dynamics of cavity quantum electrodynamics*, Academic Press, Inc., Boston, MA, 1994.
- [8] G. W. Biedermann, F. M. Benito, K. M. Fortier, D. L. Stick, T. K. Loyd, P. D. D. Schwindt, C. Y. Nakakura, R. L. Jarecki, and M. G. Blain, *Ultrasmooth microfabricated mirrors for quantum information*, Applied Physics Letters **97** (2010), no. 18, 181110 –3.
- [9] Serge Haroche and Daniel Kleppner, *Cavity Quantum Electrodynamics*, Physics Today (1989).
- [10] Serge Haroche and Jean-Michel Raimond, *Exploring the quantum atoms, cavities, and photons*, Oxford University Press, USA, 1st ed edition, 2006.
- [11] J.P. Holman, *Heat transfer*, McGraw-Hill Companies.

References

- [12] P. Horak, B.G. Klappauf, A. Haase, R. Folman, J. Schmiedmayer, P. Domokos, and E.A. Hinds, *Possibility of single-atom detection on a chip*, <http://www.scientificcommons.org/7501707> (2003).
- [13] Larry Howell, Timothy McLain, Michael Baker, and Christian Lott, *Techniques in the design of thermomechanical microactuators*, MEMS/NEMS (Cornelius T. Leondes, ed.), Springer US, 2006, 10.1007/0-387-25786-1₃₁, pp. 1177 – –1190.
- [14] ANSYS Inc., *Theory Reference for ANSYS*.
- [15] E.T. Jaynes and F.W. Cummings, *Comparison of quantum and semiclassical radiation theories with application to the beam maser*, Proc. IEEE **51** (1963), 89–109.
- [16] B. D. Jensen, M. P. de Boer, N. D. Masters, F. Bitsie, and D. A. LaVan, *Interferometry of actuated microcantilevers to determine material properties and test structure nonidealities in MEMS*, Journal of MicroElectroMechanical Systems **10** (2001), 336–346.
- [17] Marc J. Madou, *Fundamentals of microfabrication: the science of miniaturization*.
- [18] Ronald Paul Manginell, *Polycrystalline-silicon microbridge combustible gas sensor*, Ph.D. thesis, University of New Mexico, 1997.
- [19] R. Miller, T. E. Northup, K. M. Birnbaum, A. Boca, A. D. Boozer, and H. J. Kimble, *Trapped atoms in cavity QED: Coupling quantized light and matter*, Journal of Physics B: Atomic, Molecular and Optical Physics **38** (2005), 9.
- [20] Samuel L. Miller, Jeffrey J. Sniegowski, Glen LaVigne, and Paul J. McWhorter, *Friction in surface-micromachined microengines*, Proc. SPIE **2722** (1996).
- [21] Yasumasa Okada and Yozo Tokumaru, *Precise determination of lattice parameter and thermal expansion coefficient of silicon between 300 and 1500 K*, Journal of Applied Physics **56** (1984), 314–320.
- [22] T. P. Purdy and D. M. Stamper-Kurn, *Integrating cavity quantum electrodynamics and ultracold-atom chips with on-chip dielectric mirrors and temperature stabilization*, Applied Physics Letters B Lasers and Optics **90** (2008), 401–405.
- [23] Long Que, *Micromachined sensors and actuators based on bent-beam suspensions*, Ph.D. thesis, University of Wisconsin-Madison, 2000.
- [24] M. Steven Rodgers, Sridhar Kota, Joel Hetrick, Zhe Li, Brian D. Jensen, Thomas W. Krygowski, Samuel L. Miller, Stephen Matthew Barnes, and Michael Stanley Burg, *A new class of high force, low-voltage, compliant actuation system*, Technical Report SAND2000-0077C, Sandia National Labs., Albuquerque, NM (US); Sandia National Labs., Livermore, CA (US), 2000.

References

- [25] A.E. Siegman, *Lasers*, University Science Books, 1986.
- [26] T. Steinmetz, Y. Colombe, D. Hunger, T. W. Hansch, A. Balocchi, R. J. Warburton, and J Reichel, *Stable fiber-based Fabry-Perot cavity*, Applied Physics Letters **89** (2006), no. 11, 111110 – 111110–3.
- [27] M. Trupke, E. A. Hinds, S. Eriksson, E. A. Curtis, Z. Moktadir, E. Kukharenya, and M. Kraft, *Microfabricated high-finesse optical cavity with open access and small volume*, (2005).
- [28] Y. Zhu, A. Corigliano, and H. D. Espinosa, *A thermal actuator for nanoscale in situ microscopy testing: design and characterization*, Journal of Micromechanics and Microengineering **16** (2006), 242–253.